Steady-state crack growth in polymer gels: A linear poroelastic analysis

Yalin Yu, Chad M. Landis, Rui Huang*

Department of Aerospace Engineering and Engineering Mechanics, University of Texas, Austin, TX 78712, United States

A R T I C L E   I N F O

A B S T R A C T

Based on a linear poroelastic formulation, we present an asymptotic analysis of the crack tip fields for steady-state crack growth in polymer gels. A finite element method is then developed for numerical analysis. A semi-infinite crack in a long strip specimen subject to plane-strain loading is studied in detail. The crack-tip fields from the numerical analysis agree with the asymptotic analysis with a poroelastic stress intensity factor, which is generally smaller than the stress intensity factor predicted by linear elasticity due to poroelastic shielding. Similarly, the crack-tip energy release rate calculated by a modified *J*-integral method is smaller than the applied energy release rate. The size of the poroelastic crack-tip field (or *K*-field) is characterized by a diffusion length scale that is inversely proportional to the crack speed. For relatively fast crack growth, the diffusion length is small compared to the strip thickness (small-scale diffusion), and the poroelastic *K*-field transitions to an elastic *K*-field at a distance proportional to the diffusion length. In this case, the crack-tip energy release rate decreases with increasing crack speed under the same loading condition. For relatively slow crack growth, the diffusion length is greater than the strip thickness (large-scale diffusion), and the poroelastic crack-tip field is confined and transitions to a one-dimensional diffusion zone ahead of the crack tip. In this case, the energy release rate increases with increasing crack speed. Both immersed and not-immersed crack face conditions are considered. Under the same loading conditions, the poroelastic stress intensity factor and the modified *J*-integral are higher for the immersed case than not-immersed, but they approach the same values at the fast and slow crack limits. In general, if the crack-tip energy release rate is taken to be the intrinsic fracture toughness of the gel, the applied energy release rate as the apparent fracture toughness is greater due to energy dissipation associated with solvent diffusion, which is referred to as poroelastic toughening. It is proposed that the modified *J*-integral can be used to determine the intrinsic fracture toughness of the gel in experiments, which may or may not depend on crack speed. Moreover, the present results are found to be qualitatively consistent with previous experiments on the effects of solvent viscosity and crack-tip soaking.

1. Introduction

Polymer gels consist of crosslinked polymer chains and solvent molecules (e.g., water). The mechanical properties of polymer gels are similar to soft biological tissues such as tendons, ligaments, cartilage, muscles, skin, and nerves. As a result,

---

* Corresponding author.
  E-mail address: ruihuang@mail.utexas.edu (R. Huang).

polymer gels have been widely used in biomedical applications (Drury and Mooney, 2003; Langer, 2006; Peppas et al., 2006). More recently, polymer gels have also been exploited as a class of soft active materials with sensing and actuating properties in the development of soft machines and soft robotics (Calvert, 2009; Suo, 2012; Yuk et al., 2017). These applications have motivated development of tough hydrogels (Gong et al., 2003; Sun et al., 2012; Zhao, 2014) as well as fundamental studies on fracture mechanics of polymer gels (Wang and Hong, 2012; Hui et al., 2013; Lefranc and Bouchaud, 2014; Bouklas et al., 2015a; Long and Hui, 2016; Noselli et al., 2016; Long et al., 2016; Tang et al., 2017; Yang and Lin, 2018; Mao and Anand, 2018).

To enhance the facture toughness of polymer gels, a number of energy dissipation mechanisms have been employed (Zhao, 2014; Long and Hui, 2016), including both rate-insensitive damage mechanisms and rate-dependent mechanisms such as viscoelastic and poroelastic effects. The present study focuses on the poroelastic effects only, to investigate the effects of solvent diffusion on steady-state crack growth. Previously, Hui et al. (2013) studied the short time transient stress fields near the tip of a stationary crack in a poroelastic solid, based on the theory of linear poroelasticity. Bouklas et al. (2015a) proposed a modified J-integral method for calculating energy release rate of quasi-static crack growth in gels with large deformation and solvent diffusion. With a nonlinear, transient finite element method (Bouklas et al., 2015b), they studied the effects of solvent diffusion on the crack-tip fields and the energy release rate for stationary cracks in polymer gels. Noselli et al. (2016) presented a theoretical and numerical study on quasi-static, steady-state crack growth in polymer gels, also based on linear poroelasticity. They predicted a poroelastic toughening effect that is independent of crack velocity and then proposed a poroelastic cohesive zone model for the dependence of effective toughness on crack velocity. In the present study, we develop an asymptotic analysis of the crack-tip fields for steady-state crack growth in polymer gels based on linear poroelasticity and numerically show that the crack-tip energy release rate depends on crack velocity in a long strip specimen. The results are consistent with Noselli et al. (2016) at the limit of "fast" crack growth when the characteristic steady-state diffusion length scale is much smaller than the specimen size (small-scale diffusion).

Experimental measurements have reported a wide range of fracture toughness for polymer gels, from $\sim 1\,\text{J/m}^2$ for gelatin and agar gels (Forte et al., 2015; Lefranc and Bouchaud, 2014) to $\sim 9000\,\text{J/m}^2$ for a hybrid alginate-polyacrylamide gel (Sun et al., 2012). However, as noted by Long and Hui (2016), most of these measurements were interpreted by assuming that the gels are purely elastic or rate independent despite the fact that the gel typically contains over 90 wt% of water (or other solvents). Rate-dependent fracture of polymer gels may result from dynamic damage processes at the crack tip, viscoelasticity and poroelasticity. For example, Lefranc and Bouchaud (2014) attributed the crack velocity dependent toughness of agar gels to viscous chain pull-out or stress accelerated chain dynamics, both localized at the crack tip region. Wang and Hong (2012) suggested a visco-poroelastic mechanism for the delayed fracture of polymer gels that was observed in the experiments of Bonn et al. (1998). Moreover, in an experimental study on crack growth in gelatin gels, Baumberger et al. (2006) found that increasing solvent viscosity slowed crack growth, soaking the crack tip with solvent increased gel fragility, and in general, the effective fracture energy increased with crack velocity (so-called "velocity toughening"). In the present study we show that these observations are qualitatively consistent with the poroelastic model of steady-state crack growth.

The remainder of this paper is organized as follows. Section 2 presents a linear poroelastic formulation for polymer gels derived from a nonlinear theory. Section 3 describes a steady-state crack growth model. In Section 4, we develop an asymptotic analysis for the steady-state crack tip fields in a linearly poroelastic material. A finite element method is presented in Section 5, and the numerical results are discussed in Section 6. Two limiting cases (fast and slow crack growth) are presented in appendices. Section 7 concludes the present study with a brief summary.

2. A linear poroelastic formulation

The elastic deformation of the polymer network and migration of solvent molecules are generally coupled in a polymer gel. Both linear and nonlinear theories have been developed for gels. Although in general a nonlinear theory is necessary to describe large deformation of gels, a linear theory may be used as an approximation with the advantage of having possible analytical solutions. It has been shown that the generally nonlinear field theory for polymer gels (e.g., Hong et al., 2008) can be linearized for small deformation from a swollen state, leading to a linear poroelastic formulation (Bouklas and Huang, 2012). Here we summarize the linear formulation, with which an asymptotic analysis is presented for the steady-state crack-tip fields in Section 4 and a corresponding finite element method is developed in Section 5.

Let the gel be stress free and isotropically swollen in the initial state, where the solvent in the gel has a chemical potential, $\mu = \mu_0$, in equilibrium with an external solution of the same chemical potential. Relative to the dry state of the polymer network, the linear swelling ratio λ_0 of the gel in the initial state can be related to the chemical potential μ_0 as

$$N\Omega\left(\frac{1}{\lambda_0} - \frac{1}{\lambda_0^3}\right) + \ln\frac{\lambda_0^3 - 1}{\lambda_0^3} + \frac{1}{\lambda_0^3} + \frac{\chi}{\lambda_0^6} = \frac{\mu_0}{k_B T}, \tag{2.1}$$

where N is the effective number density of polymer chains in the dry state, Ω is the volume of the solvent molecule, χ is the Flory–Huggins parameter for polymer–solvent interactions, $k_B T$ is the temperature in the unit of energy with the Boltzmann constant k_B and the absolute temperature T. As in previous studies (Hong et al., 2009; Kang and Huang, 2010), the nonlinear relation is derived from the Flory–Rehner theory of polymer gels (Flory, 1953).

Now consider a displacement field u_i from the initial state. With reference to the initial state, a linear strain field can be defined as

$$\varepsilon_{ij} = \frac{1}{2}\left(\frac{\partial u_i}{\partial x_j} + \frac{\partial u_j}{\partial x_i}\right). \tag{2.2}$$

Assuming molecular incompressibility, the volumetric part of the strain is related to the change of solvent concentration, i.e.,

$$\varepsilon_{kk} = \Omega(c - c_0), \tag{2.3}$$

where $c_0 = (1 - \lambda_0^{-3})/\Omega$ is the solvent concentration in the initial state and c is the solvent concentration in the current state.

After linearization (Bouklas and Huang, 2012), the Cauchy stress in the gel is related to the strain and chemical potential as:

$$\sigma_{ij} = 2G\left[\varepsilon_{ij} + \frac{\nu}{1-2\nu}\varepsilon_{kk}\delta_{ij}\right] - \frac{\mu - \mu_0}{\Omega}\delta_{ij}, \tag{2.4}$$

where the shear modulus and Poisson's ratio are given by

$$G = \frac{1}{\lambda_0}Nk_BT, \tag{2.5}$$

$$\nu = \frac{1}{2} - \frac{N\Omega}{2}\left[\frac{1}{\lambda_0^2(\lambda_0^3 - 1)} + \frac{N\Omega}{\lambda_0^2} - \frac{2\chi}{\lambda_0^5}\right]^{-1}. \tag{2.6}$$

The linearized mechanical equilibrium equation (assuming no body force and neglecting inertial effects) is:

$$\frac{\partial \sigma_{ij}}{\partial x_j} = 0, \tag{2.7}$$

and the linearized rate equation for solvent concentration is:

$$\frac{\partial c}{\partial t} + \frac{\partial j_k}{\partial x_k} = 0, \tag{2.8}$$

where the flux vector is related to the gradient of chemical potential by a linearized kinetic law:

$$j_k = -M_0\frac{\partial \mu}{\partial x_k}, \tag{2.9}$$

with a constant mobility

$$M_0 = \frac{D}{\Omega k_BT}\frac{\lambda_0^3 - 1}{\lambda_0^3}, \tag{2.10}$$

and D is solvent diffusivity in the gel.

The linearized boundary conditions for tractions and solvent flux are:

$$\sigma_{ij}n_j = \tau_i \text{ and } j_kn_k = -i \tag{2.11}$$

where n_j is the outward normal unit vector on the boundary, τ_i is the traction, and i is the in-flux rate of the solvent across the boundary.

The linearized equations can be further reduced by inserting (2.2) into (2.4) and then into (2.7) so that:

$$\frac{\partial^2 u_i}{\partial x_j \partial x_j} + \frac{1}{1-2\nu}\frac{\partial^2 u_j}{\partial x_j \partial x_i} = \frac{1}{G\Omega}\frac{\partial \mu}{\partial x_i}, \tag{2.12}$$

which leads to: $\nabla^2\mu = \frac{2(1-\nu)}{1-2\nu}\Omega^2 G\nabla^2 c$, as a result of Eq. (2.3). Substituting (2.12) into (2.9) and then into Eq. (2.8), we obtain

$$\frac{\partial c}{\partial t} = D^*\nabla^2 c, \tag{2.13}$$

where $D^* = \frac{2(1-\nu)}{1-2\nu}\Omega^2 GM_0$ is often called the effective or cooperative diffusivity (Hui et al., 2006; Hu et al., 2011; Bouklas and Huang, 2012). As with all standard diffusion equations, (2.13) implies a time-dependent length scale:

$$l_t = \sqrt{D^*t}. \tag{2.14}$$

The above linear poroelastic formulation is essentially identical to Biot's theory of linear poroelasticity (Biot, 1941), with a pore pressure proportional to the change of chemical potential ($\mu - \mu_0$) and Darcy's law equivalent to Eq. (2.9).
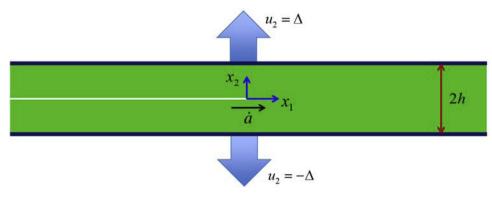
Fig. 1. Schematic of a long strip specimen with steady-state crack growth in the x_1 direction.

As in linear elasticity, the equilibrium Eq. (2.7) may be solved by using a stress function under plane-strain or plane-stress conditions. However, the poroelastic stress-strain relation in Eq. (2.4) leads to a slightly different compatibility condition in terms of the stress function, namely

$$\nabla^2\nabla^2\varphi = -2\Omega G\nabla^2 c, \tag{2.15}$$

where Airy's stress function φ is related to the stress components as usual: $\sigma_\theta = \frac{\partial^2\varphi}{\partial r^2}$, $\sigma_{\theta r} = -\frac{\partial}{\partial r}(\frac{1}{r}\frac{\partial\varphi}{\partial\theta})$, and $\sigma_r = \frac{1}{r}\frac{\partial\varphi}{\partial r} + \frac{1}{r^2}\frac{\partial^2\varphi}{\partial\theta^2}$.

Eq. (2.4) leads to a relation between the chemical potential, solvent concentration, and the hydrostatic stress:

$$\sigma_{kk} = \frac{2\Omega G(1+\nu)}{1-2\nu}(c-c_0) - \frac{3}{\Omega}(\mu-\mu_0). \tag{2.16}$$

For plane stress ($\sigma_z = 0$), $\sigma_{kk} = \nabla^2\varphi$ so that the chemical potential can be obtained as

$$\mu-\mu_0 = \frac{2(1+\nu)G\Omega^2}{3(1-2\nu)}(c-c_0) - \frac{\Omega}{3}\nabla^2\varphi. \tag{2.17}$$

For plane strain ($\varepsilon_z = 0$), $\sigma_{kk} = \nabla^2\varphi + \sigma_z$ and $\sigma_z = \frac{2\nu}{1-2\nu}G\Omega(c-c_0) - \frac{\mu-\mu_0}{\Omega}$ so that

$$\mu-\mu_0 = \frac{G\Omega^2}{1-2\nu}(c-c_0) - \frac{\Omega}{2}\nabla^2\varphi. \tag{2.18}$$

Therefore, we may solve Eq. (2.13) for the solvent concentration and then solve Eq. (2.15) for the stress function, with which both the stress and chemical potential fields can be determined under the plane-strain or plane-stress conditions.

3. A plane-strain steady-state crack growth model

In the present study, we consider steady-state crack growth in a long strip specimen of a polymer gel (Fig. 1). The initial state of the gel is stress free and homogeneously swollen, with a solvent concentration $c_0 = (1-\lambda_0^{-3})/\Omega$ corresponding to the chemical potential $\mu_0 = 0$ by Eq. (2.1). The strip thickness is $2h$, with a semi-infinite crack lying in the middle plane. Subject to an opening displacement $\pm\Delta$ applied to the upper and lower surfaces of the strip, the crack grows and reaches a steady state with a constant crack speed $\dot{a}$. Similar specimens and setups have been used in experiments for various materials including gels (Rivlin and Thomas, 1953; Baumberger et al., 2006).[1]

A moving coordinate system is adopted such that the crack tip lies at the origin and $\mathbf{x}(t) = \mathbf{x}(0) - \dot{a}t\mathbf{e}_1$, where x(0) is the fixed (initial) coordinate at $t=0$ and $\mathbf{e}_1$ is the unit vector in the direction of crack growth. Then, with respect to the moving coordinate, the mechanical equilibrium equation remains the same as in Eq. (2.7). The rate equation for the solvent concentration becomes time-independent for the steady-state crack growth as $\frac{\partial}{\partial t}|_{x(0)} = -\dot{a}\frac{\partial}{\partial x_1}$, and hence Eq. (2.13) becomes

$$-\dot{a}\frac{\partial c}{\partial x_1} = D^*\nabla^2 c. \tag{3.1}$$

A steady-state diffusion length scale emerges from Eq. (3.1):

$$l_{SS} = \frac{D^*}{\dot{a}}, \tag{3.2}$$

---

[1] Most experiments use thin sheets under plane stress conditions with the top and bottom gripped so that the displacements are fixed in both x_1 and x_2 directions. It is commonly known as the pure shear test. Under plane strain conditions, however, we have to relax the displacement in the x_1 direction because otherwise the gel cannot be stretched ahead of the crack tip due to incompressibility.

which is inversely proportional to the crack speed.

Eq. (3.1) is to be solved along with Eq. (2.15) for the steady-state crack problem. The long strip model (Fig. 1) has two relevant length scales: the half-thickness h and the steady-state diffusion length l_{SS}. The ratio between the two length scales defines a dimensionless number

$$Pe = \frac{h}{l_{SS}} = \frac{\dot{a}h}{D^*},$$ (3.3)

which is commonly called the Péclet number for advection–diffusion problems in fluid mechanics (Franca et al., 1992). Eq. (3.1) takes the same form as the stationary advection–diffusion equation, with an advection velocity $\mathbf{v} = -\dot{a}\mathbf{e_1}$ and diffusivity D^*. With respect to the moving coordinate, the advection velocity is opposite to the crack velocity.

By dimensional considerations, the solution for the steady-state crack problem depends on three dimensionless parameters: the Péclet number (Pe), Poisson's ratio (ν), and the loading strain ($\varepsilon_\infty = \Delta/h$). Within the linear formulation, the stress field, the chemical potential ($\mu - \mu_0$), and the solvent concentration ($c - c_0$) are all linearly proportional to the loading strain ε_∞. The dependence on the Péclet number arises for a finite specimen thickness due to crack-tip solvent diffusion zone interacting with the specimen boundary (hence large-scale diffusion).

To calculate the crack-tip energy release rate in poroelastic gels, a modified J-integral was derived by Bouklas et al., (2015a) in a nonlinear setting, which can be linearized to yield:

$$J^* = \int_{C_1} \left(\hat{\phi} n_1 - \sigma_{ij} n_j \frac{\partial u_i}{\partial x_1} \right) d\Gamma + \int_{A_1} (c - c_0) \frac{\partial \mu}{\partial x_1} dA,$$ (3.4)

where A_1 is the area enclosed by the contour C_1 around the crack tip and the linearized free energy density function is

$$\hat{\phi} = G \left[\varepsilon_{ij} \varepsilon_{ij} + \frac{\nu}{1 - 2\nu} (\varepsilon_{kk})^2 \right] - (\mu - \mu_0)(c - c_0).$$ (3.5)

Note that the linearized J-integral in Eq. (3.4) gives the energy release rate per unit area of crack growth in the initial swollen state, not in the dry state as in the original definition by Bouklas et al. (2015a); the two are simply related by a factor of λ_0^2. By dimensional consideration, $J^* \sim G\varepsilon_\infty^2 h$, with a proportionality depending on the Péclet number (Pe) and Poisson's ratio (ν).

If the long strip specimen is made of a material that is linearly elastic and incompressible ($\nu_\infty = 0.5$, with no solvent diffusion), the energy release rate for the steady state crack growth can be obtained simply by comparing the elastic strain energy far ahead of the crack tip with that far behind the crack tip, namely

$$J_e = 4G\varepsilon_\infty^2 h$$ (3.6)

which is independent of the crack speed.[2] Correspondingly, the stress intensity factor at the crack tip is:

$$K_e = 4G\varepsilon_\infty \sqrt{h}.$$ (3.7)

For a poroelastic specimen, however, part of the elastic energy is dissipated due to solvent diffusion around the crack tip. Consequently, the crack-tip energy release rate by the modified J-integral in Eq. (3.4) is generally lower than the applied energy release rate in Eq. (3.6) and may depend on the crack speed, as discussed further in Section 6. Similarly, the stress intensity factor in a linearly poroelastic specimen is generally lower than Eq. (3.7), an effect known as poroelastic shielding (Atkinson and Craster, 1991; Hui et al., 2013).

4. Asymptotic steady-state crack-tip fields

In this section we solve Eqs. (3.1) and (2.15) to obtain an asymptotic solution for the steady-state crack-tip fields in a linearly poroelastic material. First, to solve Eq. (3.1) near the crack tip, we assume

$$c - c_0 = c_1 + \frac{1}{\Omega} \sum_n \left(\frac{r}{l_{SS}} \right)^n f_n(\theta),$$ (4.1)

where r and θ are the polar coordinates with the origin at the crack tip; c_1 is a constant term (a trivial solution to Eq. (3.1)) in addition to the initial solvent concentration c_0. The constant term is associated with the T-stress at the crack tip. Note that, since $\varepsilon_{kk} = \Omega(c - c_0)$, $n > -1$ is required in Eq. (4.1) so that the displacement remains finite at the crack tip as $r \to 0$. Substitution of Eq. (4.1) into Eq. (3.1) leads to a recursive equation:

$$n^2 f_n(\theta) + f_n''(\theta) = -(n - 1) f_{n-1}(\theta) \cos\theta + f_{n-1}'(\theta) \sin\theta.$$ (4.2)

For the crack-tip field as $r \to 0$, the most singular term corresponds to the minimum value of n (designated as m), for which the right-hand side of Eq. (4.2) must vanish, i.e.,

$$f_m''(\theta) + m^2 f_m(\theta) = 0.$$ (4.3)

---

[2] This is the same for the pure shear test under the plane stress condition, assuming the material to be linearly elastic and incompressible. For both plane strain and plane stress, the strain far ahead of the crack tip is biaxial, with $\varepsilon_{33} = 0$ for plane strain and $\varepsilon_{11} = 0$ for plane stress (pure shear).

Solving Eq. (4.3) yields a solution:

$$f_m(\theta) = A_m \cos(m\theta) + B_m \sin(m\theta). \tag{4.4}$$

The next term in the series expansion can then be obtained by solving Eq. (4.2) with $n = m + 1$, which yields

$$f_{m+1}(\theta) = -\frac{1}{4}A_m \cos(m-1)\theta - \frac{1}{4}B_m \sin(m-1)\theta + A_{m+1}\cos(m+1)\theta + B_{m+1}\sin(m+1)\theta. \tag{4.5}$$

Following the same procedure, we may obtain the higher order terms ($n > m + 1$) in Eq. (4.1) recursively.
With Eq. (4.1) for the solvent concentration (to the leading orders with $n = m$ and $m + 1$), Eq. (2.15) becomes

$$\nabla^2\nabla^2\varphi = \frac{2mG}{l_{SS}^2}[A_m \cos(m-1)\theta + B_m \sin(m-1)\theta]\left(\frac{r}{l_{SS}}\right)^{m-1}. \tag{4.6}$$

The general solution to Eq. (4.6) consists of a particular solution and a homogeneous solution, namely

$$\varphi = \varphi_h(r,\theta) + \frac{Gl_{SS}^2}{16(m+1)}\left(\frac{r}{l_{SS}}\right)^{m+3}[A_m \cos(m-1)\theta + B_m \sin(m-1)\theta], \tag{4.7}$$

where the homogenous solution takes the form of a series expansion as:

$$\varphi_h(r,\theta) = \sum_{n=0}^{\infty} \phi_n(\theta)\left(\frac{r}{l_{SS}}\right)^{\frac{n+3}{2}}, \tag{4.8}$$

$$\varphi_n(\theta) = C_{n1}\cos\left(\frac{n+3}{2}\theta\right) + C_{n2}\sin\left(\frac{n+3}{2}\theta\right) + C_{n3}\cos\left(\frac{n-1}{2}\theta\right) + C_{n4}\sin\left(\frac{n-1}{2}\theta\right). \tag{4.9}$$

The stress field associated with the particular solution is non-singular, $\sigma \sim r^{m+1}$ ($m > -1$), but the leading term of the homogeneous solution ($n = 0$) leads to a singular stress field with $\sigma \sim r^{-1/2}$, which is the same as that in the linear elastic crack-tip solution.

The asymptotic solution in the form of Eqs. (4.1) and (4.7) can be decomposed into symmetric (mode I) and anti-symmetric (mode II) modes with respect to the angular variations. Hereafter, we consider only the solution for cracks in the symmetric mode (mode I) under plane strain conditions. By inserting Eqs. (4.1) and (4.7) into (2.18), we obtain the chemical potential:

$$\begin{aligned}
\mu(r,\theta) = &-\frac{\Omega}{l_{SS}^2}\left(\frac{r}{l_{SS}}\right)^{-1/2}C_{03}\cos\left(\frac{\theta}{2}\right) + \frac{\Omega G}{1-2v}\left(\frac{r}{l_{SS}}\right)^m A_m \cos(m\theta) \\
&-\frac{\Omega}{2l_{SS}^2}\sum_{n=1}^{\infty}\hat{\varphi}_n(\theta)\left(\frac{r}{l_{SS}}\right)^{\frac{n-1}{2}} + \frac{G\Omega^2}{1-2v}c_1 \\
&-\frac{\Omega G}{4}\left(\frac{r}{l_{SS}}\right)^{m+1}\left[\frac{2(1-v)}{1-2v}A_m\cos(m-1)\theta - \frac{4}{1-2v}A_{m+1}\cos(m+1)\theta\right]
\end{aligned} \tag{4.10}$$

where $\hat{\varphi}_1(\theta) = 4C_{13}$ and $\hat{\varphi}_2(\theta) = 6C_{23}\cos(\frac{\theta}{2})$; the terms of higher order than these are ignored.

If the crack is filled with an external solution (e.g., water), the chemical potential at the crack faces ($\theta = \pm\pi$) equals a constant, i.e., $\mu = 0$, and such a crack is called *immersed*. Alternatively, if the crack is *not-immersed*, we assume that the crack faces are impermeable to solvent diffusion so that the flux across the crack faces is zero, i.e., $\frac{\partial\mu}{\partial\theta} = 0$. Consider the case of an immersed crack first. Clearly, the first term on the right hand side of Eq. (4.10) satisfies the immersed boundary condition at the crack faces. For the second term, if $A_m \neq 0$, the boundary condition requires that $m = \pm\frac{1}{2}, \pm\frac{3}{2}, \dots$ Since $m > -1$, the most singular term must correspond to $m = -\frac{1}{2}$. Therefore, the leading terms for the solvent concentration in Eq. (4.1) are:

$$(c - c_0)\Omega = A_m\cos\left(\frac{\theta}{2}\right)\left(\frac{r}{l_{SS}}\right)^{-1/2} + c_1\Omega + \left[-\frac{1}{4}A_m\cos\left(\frac{3\theta}{2}\right) + A_{m+1}\cos\left(\frac{\theta}{2}\right)\right]\left(\frac{r}{l_{SS}}\right)^{1/2}. \tag{4.11}$$

Thus, the two singular terms in Eq. (4.10) for the chemical potential result from the singular stress field and the singular solvent concentration, respectively. However, the chemical potential should remain finite at the crack tip, which requires the two singular terms to cancel out. Consequently, we must have

$$A_m = \frac{1-2v}{Gl_{SS}^2}C_{03}. \tag{4.12}$$

The next terms in Eq. (4.10) are associated with $n = 1$ and c_1, which are both independent of r or θ. To satisfy the immersed boundary condition at the crack faces ($\theta = \pm\pi$), we must have $C_{13} = \frac{Gl_{SS}^2}{2(1-2v)}\Omega c_1$ so that the two constant terms

cancel out. Therefore, the leading term of the chemical potential for an immersed crack must be proportional to $r^{1/2}$, with contributions from both the solvent concentration ($m = -\frac{1}{2}$) and the stress field ($n = 2$), such that:

$$\mu = -\frac{\Omega G}{4}\left[\frac{2(1-\nu)}{1-2\nu}A_m\cos\left(\frac{3\theta}{2}\right) - \frac{4}{1-2\nu}A_{m+1}\cos\left(\frac{\theta}{2}\right) + \frac{12C_{23}}{Gl_{SS}^2}\cos\left(\frac{\theta}{2}\right)\right]\left(\frac{r}{l_{SS}}\right)^{1/2}. \tag{4.13}$$

To satisfy the traction boundary conditions, we obtain the stress components as:

$$\sigma_\theta = \frac{\partial^2\varphi}{\partial r^2} = \frac{3}{4l_{SS}^2}\left[C_{01}\cos\left(\frac{3\theta}{2}\right) + C_{03}\cos\left(\frac{\theta}{2}\right)\right]\left(\frac{r}{l_{SS}}\right)^{-1/2} + \frac{2}{l_{SS}^2}[C_{11}\cos(2\theta) + C_{13}]$$

$$+ \frac{15G}{32}A_m\cos\left(\frac{3\theta}{2}\right)\left(\frac{r}{l_{SS}}\right)^{1/2} + \frac{15}{4l_{SS}^2}\varphi_2(\theta)\left(\frac{r}{l_{SS}}\right)^{1/2} \tag{4.14}$$

$$\sigma_{\theta r} = -\frac{\partial}{\partial r}\left(\frac{1}{r}\frac{\partial\varphi}{\partial\theta}\right) = \frac{1}{4l_{SS}^2}\left[3C_{01}\sin\left(\frac{3\theta}{2}\right) + C_{03}\sin\left(\frac{\theta}{2}\right)\right]\left(\frac{r}{l_{SS}}\right)^{-1/2} + \frac{2}{l_{SS}^2}C_{11}\sin(2\theta) \tag{4.15}$$

$$+ \frac{9G}{32}A_m\sin\left(\frac{3\theta}{2}\right)\left(\frac{r}{l_{SS}}\right)^{1/2} - \frac{3}{2l_{SS}^2}\varphi'_2(\theta)\left(\frac{r}{l_{SS}}\right)^{1/2} \tag{4.15}$$

where $C_{03} = 3C_{01}$ is required for the singular terms to satisfy the traction-free condition on the crack faces ($\theta = \pm\pi$). The second term in Eq. (4.14) is associated with the T-stress, for which $C_{11} = -C_{13}$ is required to satisfy the traction-free condition on the crack faces. As a result, the T-stress can be related to the constant term in the solvent concentration as: $T = \frac{4C_{13}}{l_{SS}^2} = \frac{2G\Omega c_1}{1-2\nu}$.

Following linear elastic fracture mechanics (LEFM), the singular part of the asymptotic crack-tip stress field may be written as:

$$\sigma_\theta = \frac{K_I}{\sqrt{2\pi r}}\left[\frac{3}{4}\cos\left(\frac{\theta}{2}\right) + \frac{1}{4}\cos\left(\frac{3\theta}{2}\right)\right], \tag{4.16}$$

$$\sigma_r = \frac{K_I}{\sqrt{2\pi r}}\left[\frac{5}{4}\cos\left(\frac{\theta}{2}\right) - \frac{1}{4}\cos\left(\frac{3\theta}{2}\right)\right], \tag{4.17}$$

$$\sigma_{\theta r} = \frac{K_I}{\sqrt{2\pi r}}\left[\frac{1}{4}\sin\left(\frac{\theta}{2}\right) + \frac{1}{4}\sin\left(\frac{3\theta}{2}\right)\right], \tag{4.18}$$

where $K_I = \frac{C_{03}}{l_{SS}^2}\sqrt{2\pi l_{SS}}$ is the mode-I stress intensity factor. Therefore, the singular stress field is characterized by a single parameter, K_I, while the singular concentration field in Eq. (4.11) is characterized by A_m. The two are related via Eq. (4.12):

$$A_m = \frac{1-2\nu}{G\sqrt{2\pi l_{SS}}}K_I. \tag{4.19}$$

To summarize, we have obtained a linear poroelastic solution for the asymptotic steady-state crack-tip fields (mode I) as follows:

$$(c - c_0)\Omega = \frac{(1-2\nu)K_I}{G\sqrt{2\pi r}}\cos\left(\frac{\theta}{2}\right) + c_1\Omega + o\left(\sqrt{\frac{r}{l_{SS}}}\right), \tag{4.20}$$

$$\sigma_{ij} = \frac{K_I}{\sqrt{2\pi r}}f_{ij}(\theta) + T\delta_{1i}\delta_{1j} + o\left(\sqrt{\frac{r}{l_{SS}}}\right), \tag{4.21}$$

where

$$f_{11} = \cos\left(\frac{\theta}{2}\right)\left[1 - \sin\left(\frac{\theta}{2}\right)\sin\left(\frac{3\theta}{2}\right)\right], \tag{4.22}$$

$$f_{22} = \cos\left(\frac{\theta}{2}\right)\left[1 + \sin\left(\frac{\theta}{2}\right)\sin\left(\frac{3\theta}{2}\right)\right], \tag{4.23}$$

$$f_{12} = \cos\left(\frac{\theta}{2}\right)\sin\left(\frac{\theta}{2}\right)\cos\left(\frac{3\theta}{2}\right), \tag{4.24}$$

$$T = \frac{2G}{1-2v}\Omega c_1. \tag{4.25}$$

The chemical potential in Eq. (4.13) can be re-written as

$$\mu = -\frac{(1-v)\Omega K_I}{2\sqrt{2\pi l_{SS}}}\left[\cos\left(\frac{3\theta}{2}\right) + \kappa\cos\left(\frac{\theta}{2}\right)\right]\left(\frac{r}{l_{SS}}\right)^{1/2} + o\left(\frac{r}{l_{SS}}\right), \tag{4.26}$$

where $\kappa = (\frac{12C_{23}}{Gl_{SS}^2} - \frac{4A_{m+1}}{1-2v})\frac{G\sqrt{2\pi l_{SS}}}{2(1-v)K_I}$. Thus, the leading term of the chemical potential field depends on the stress intensity factor K_I and an additional parameter, κ. The latter has an effect on the angular distribution of the chemical potential around the crack tip, which in turn would also influence diffusion flux and energy dissipation.

We note that the leading terms of the present solution are identical to those obtained by Noselli et al. (2016). In addition, we obtain a relationship between the T-stress and the constant term of solvent concentration. As a result, three independent parameters are needed to describe the poroelastic crack-tip fields for the immersed case: K_I, T and κ. A similar solution was also obtained by Atkinson and Craster (1991) using a Fourier transform method.

Furthermore, the asymptotic crack-tip strain field can be obtained from Eq. (2.4). The singular part of the strain field is identical to that in the linear elastic solution, namely

$$\varepsilon_{11} = \frac{1}{2G}\frac{K_I}{\sqrt{2\pi r}}\cos\left(\frac{\theta}{2}\right)\left[1 - 2v - \sin\left(\frac{\theta}{2}\right)\sin\left(\frac{3\theta}{2}\right)\right] + \frac{(1-v)T}{2G} + o\left(\sqrt{\frac{r}{l_{SS}}}\right), \tag{4.27}$$

$$\varepsilon_{22} = \frac{1}{2G}\frac{K_I}{\sqrt{2\pi r}}\cos\left(\frac{\theta}{2}\right)\left[1 - 2v + \sin\left(\frac{\theta}{2}\right)\sin\left(\frac{3\theta}{2}\right)\right] - \frac{vT}{2G} + o\left(\sqrt{\frac{r}{l_{SS}}}\right), \tag{4.28}$$

$$\varepsilon_{12} = \frac{1}{2G}\frac{K_I}{\sqrt{2\pi r}}\cos\left(\frac{\theta}{2}\right)\sin\left(\frac{\theta}{2}\right)\cos\left(\frac{3\theta}{2}\right) + o\left(\sqrt{\frac{r}{l_{SS}}}\right). \tag{4.29}$$

Thus, the leading term of the displacement field is also identical to the linear elastic solution. In particular, the crack opening displacement is given by:

$$u_2(r, \theta = \pm\pi) = \pm\frac{2(1-v)K_I}{G}\sqrt{\frac{r}{2\pi}} + o\left(\frac{r}{l_{SS}}\right). \tag{4.30}$$

The free energy density function in Eq. (3.5) is obtained as:

$$\hat{\phi} = \frac{K_I^2}{4\pi Gr}\cos^2\left(\frac{\theta}{2}\right)\left[(1-2v) + \sin^2\left(\frac{\theta}{2}\right)\right] + o\left(\sqrt{\frac{l_{SS}}{r}}\right). \tag{4.31}$$

Then, the J-integral in Eq. (3.4) can be calculated with a circular contour of radius r as:

$$J^* = J_\Gamma(r) + J_A(r), \tag{4.32}$$

where

$$J_\Gamma(r) = \int_\Gamma\left(\hat{\phi}n_1 - \sigma_{ij}n_j\frac{\partial u_i}{\partial x_1}\right)d\Gamma = J_{tip} + o\left(\sqrt{\frac{r}{l_{SS}}}\right), \tag{4.33}$$

$$J_A(r) = \int_A(c - c_0)\frac{\partial\mu}{\partial x_1}dA = o\left(\frac{r}{l_{SS}}\right). \tag{4.34}$$

As shown in the previous study (Bouklas et al., 2015a), the modified J-integral (J^*) is path independent whereas the classical J-integral (J_Γ) is not; the two integrals converge as the contour shrinks towards the crack tip, i.e., $J^* = J_\Gamma(r \to 0) = J_{tip}$ and $J_A(r \to 0) = 0$. Thus, the relationship between the modified J-integral and the stress intensity factor is identical to that in LEFM, namely

$$J^* = \frac{(1-v)K_I^2}{2G}. \tag{4.35}$$

We note that the domain integral in Eq. (4.34) is typically negative as a result of energy dissipation by solvent diffusion within the domain, whereas the contour integral in Eq. (4.33) is the total energy supply into the domain. By subtracting the dissipated energy from the total energy, the modified J-integral in Eq. (4.32) gives the energy release rate of crack growth in a poroelastic material; see Bouklas et al. (2015a) for a detailed derivation.

If the crack face is impermeable to solvent diffusion, the zero chemical potential condition is replaced by the zero-flux condition for a not-immersed crack. In this case, Eq. (4.10) dictates that the most singular term for the solvent concentration corresponds to $m = -\frac{1}{2}$ as well, in order for the chemical potential to be finite at the crack tip. Therefore, the leading terms for the solvent concentration remain the same as in Eq. (4.11), and Eq. (4.12) holds as well. However, unlike the immersed

case, the leading terms for the chemical potential are associated with $n = 1$ and c_1 in Eq. (4.10), which do not cancel out under the zero-flux condition:

$$\mu = \mu_{tip} - \frac{(1-\nu)\Omega K_I}{2\sqrt{2\pi l_{SS}}} \left[\cos\left(\frac{3}{2}\theta\right) + \kappa \cos\left(\frac{\theta}{2}\right) \right] \left(\frac{r}{l_{SS}}\right)^{1/2} + o\left(\frac{r}{l_{SS}}\right), \tag{4.36}$$

where

$$\mu_{tip} = \frac{G\Omega^2}{1-2\nu}c_1 - \frac{1}{2}\Omega T. \tag{4.37}$$

To satisfy the zero-flux crack face condition, it requires that $\kappa = 3$ in Eq. (4.36). The stress field remains the same as given by Eq. (4.21), except that the T-stress in this case is not related to c_1 by Eq. (4.25). The poroelastic crack-tip fields in this case are then characterized by three independent parameters: K_I, T, and c_1 (or μ_{tip}). It can be shown that the modified J-integral in this case is also path-independent, and Eq. (4.35) holds as well.

5. Finite element method

In this section we present a finite element method for numerical simulations of the steady-state crack growth based on the linear poroelastic formulation.

5.1. Weak form

The solution to the steady-state boundary value problem consists of a vector field of displacement and a scalar field of chemical potential, $\mathbf{u}(\mathbf{x})$ and $\mu(\mathbf{x})$. Similar to previous work (Bouklas et al., 2015b), the weak form of Eqs. (2.7) and (2.8) (replacing $\partial c/\partial t$ with $-\dot{a}\partial c/\partial x_1$ for the steady state) is obtained by using the test functions $\delta\mathbf{u}(\mathbf{x})$ and $\delta\mu(\mathbf{x})$ with the divergence theorem, namely

$$\int_{V_0} \sigma_{ij}\delta u_{i,j}dV = \oint_{S_0} \tau_i \delta u_i dS, \tag{5.1}$$

$$\int_{V_0} \left(c\delta_{1k} - \frac{1}{\dot{a}}j_k\right)\delta\mu_{,k}dV = \oint_{S_0} \left(cn_1 + \frac{1}{\dot{a}}i\right)\delta\mu dS. \tag{5.2}$$

Hence, the weak form of the boundary value problem is to find $\mathbf{u}(\mathbf{x})$ and $\mu(\mathbf{x})$ such that the integral equations are satisfied for any admissible test functions, $\{\delta\mathbf{u}(\mathbf{x}), \delta\mu(\mathbf{x})\}$.

5.2. Discretization

The displacement field and the chemical potential are discretized as:

$$\mathbf{u} = \mathbf{N}^u\mathbf{u}^n \text{ and } \mu - \mu_0 = \mathbf{N}^\mu\boldsymbol{\mu}^n \tag{5.3}$$

where $\mathbf{N}^u$ and $\mathbf{N}^\mu$ are the corresponding shape functions for the displacements and the chemical potential, respectively, $\mathbf{u}^n$ and $\boldsymbol{\mu}^n$ are the nodal values. Following the standard Galerkin method, the test functions are discretized in the same way:

$$\delta\mathbf{u} = \mathbf{N}^u\delta\mathbf{u}^n \text{ and } \delta\mu = \mathbf{N}^\mu\delta\boldsymbol{\mu}^n \tag{5.4}$$

The stress, solvent concentration and flux are evaluated at the integration points using Eqs. (2.2)–(2.4) and (2.9). Taking the gradients of the discretized displacements and chemical potential, we obtain

$$\nabla\mathbf{u} = \mathbf{B}^u\mathbf{u}^n \text{ and } \nabla\mu = \mathbf{B}^\mu\boldsymbol{\mu}^n \tag{5.5}$$

where $\mathbf{B}^u$ and $\mathbf{B}^\mu$ are the gradients of the corresponding shape functions for the displacement and chemical potential fields. In this formulation, different shape functions are allowed for the discretization of the displacement and chemical potential. Following previous work (Bouklas et al., 2015b), the 8$\mathbf{u}$4p Taylor–Hood elements with biquadratic serendipity interpolation for displacement and bilinear interpolation for chemical potential are used to alleviate numerical oscillations.

Upon discretization, the weak form in (5.1) and (5.2) leads to a system of linear equations:

$$\mathbf{Kd} = \mathbf{f}, \tag{5.6}$$

where $\mathbf{d} = \begin{bmatrix} \mathbf{u}^n \\ \boldsymbol{\mu}^n \end{bmatrix}$ is a vector of the nodal displacements and chemical potentials, $\mathbf{f} = \begin{bmatrix} \mathbf{f}^u \\ \mathbf{f}^\mu \end{bmatrix}$ is the external force vector, and $\mathbf{K}$ is the stiffness matrix. Specifically, the external force components are given by

$$f_i^{u,m} = \int_{S_0} \tau_i N^{u,m} dS, \tag{5.7}$$

$$f^{\mu,m} = \frac{1}{\dot{a}} \int_{S_0} iN^{\mu,m} dS, \tag{5.8}$$

where m indicates the node. The stiffness matrix can be written as

$$\mathbf{K} = \begin{bmatrix} \mathbf{K}^{uu} & \mathbf{K}^{u\mu} \\ \mathbf{K}^{\mu u} & \mathbf{K}^{\mu\mu} \end{bmatrix},$$ (5.9)

where the components are:

$$K_{ik}^{uu,mn} = \int_{V_0} B_j^{u,m} \frac{\partial \sigma_{ij}}{\partial u_{k,l}} B_l^{u,n} dV,$$ (5.10a)

$$K_i^{u\mu,mn} = -\frac{1}{\Omega} \int_{V_0} B_i^{u,m} N^{\mu,n} dV,$$ (5.10b)

$$K_i^{\mu u,mn} = \frac{1}{\Omega} \left(\int_{V_0} B_1^{\mu,m} B_i^{u,n} dV - \int_{S_0} N^{\mu,m} B_i^{u,n} n_1 dS \right),$$ (5.10c)

$$K^{\mu\mu,mn} = \frac{M_0}{\dot{a}} \int_{V_0} B_i^{\mu,m} B_i^{\mu,n} dV.$$ (5.10d)

In Eq. (5.10a), the derivative of stress is the isotropic elasticity tensor, namely

$$\frac{\partial \sigma_{ij}}{\partial u_{k,l}} = G \left(\delta_{ik} \delta_{jl} + \delta_{il} \delta_{jk} + \frac{2\nu}{1-2\nu} \delta_{ij} \delta_{kl} \right).$$ (5.11)

For purely elastic problems, we only have $\mathbf{K}^{uu}$, which is symmetric and positive definite; similarly, $\mathbf{K}^{\mu\mu}$ is also symmetric and positive definite. However, with the coupling terms, $\mathbf{K}^{u\mu}$ and $\mathbf{K}^{\mu u}$, the stiffness matrix in Eq. (5.9) is generally not symmetric for the coupled poroelasticity problem. An open-source package PETSc is used to solve the asymmetric linear equations by LU decomposition (Balay et al., 2017).

5.3. Numerical stabilization

As noted in Section 3, Eq. (3.1) takes the same form as the stationary advection-diffusion equation in fluid mechanics (Franca et al., 1992), for which the solution depends on the dimensionless Péclet number as defined in Eq. (3.3). When the Péclet number is high, the advection term dominates over the diffusion term, which may lead to spurious node-to-node oscillations for the standard Galerkin method (Johnson, 1987). The numerical oscillations may be partly eliminated by refining the mesh, which can significantly increase the computational cost. To preclude such numerical oscillations, many stabilization techniques have been developed (Franca et al., 2006), among which the consistent streamline-upwind-Petrov-Galerkin (SUPG) method (Brooks and Hughes, 1982) is commonly used. Here, we adopt the SUPG method for numerical stabilization.

Unlike the standard Galerkin method, which uses the same discretization for the test function, i.e., $\delta\mu = \mathbf{N}^\mu \delta\boldsymbol{\mu}^n$, the SUPG method (Brooks and Hughes, 1982; Franca et al., 2006) uses a different discretization for the test function:

$$\delta\mu^* = \delta\mu + \tau \mathbf{v} \cdot \nabla(\delta\mu) = (\mathbf{N}^\mu + \tau \mathbf{v} \cdot \nabla \mathbf{N}^\mu)\delta\boldsymbol{\mu}^n,$$ (5.12)

where τ is called the stabilization parameter. For each element, the local Péclet number depends on the element size and so does the stabilization parameter. For a 2D quadrilateral element (Fig. 2), the stabilization parameter τ^e is calculated as (Brooks and Hughes, 1982)

$$\tau^e = \frac{1}{2|\mathbf{v}|^2} \left(\alpha_\xi v_\xi h_\xi + \alpha_\eta v_\eta h_\eta \right),$$ (5.13)

where ξ and η are the local coordinates with the unit vector $\mathbf{e}_\xi$ and $\mathbf{e}_\eta$ as shown in Fig. 2, h_ξ and h_η are characteristic element sizes in the two directions, $v_\xi = \mathbf{v} \cdot \mathbf{e}_\xi$ and $v_\eta = \mathbf{v} \cdot \mathbf{e}_\eta$, and

$$\alpha_\xi = \coth\left(\frac{v_\xi h_\xi}{2D^*}\right) - \frac{2D^*}{v_\xi h_\xi},$$ (5.14)

$$\alpha_\eta = \coth\left(\frac{v_\eta h_\eta}{2D^*}\right) - \frac{2D^*}{v_\eta h_\eta}.$$ (5.15)

As a result, the weak form in Eq. (5.2) becomes (with $\mathbf{v} = -\dot{a}\mathbf{e_1}$)

$$\int_{V_0} \left(c\delta_{1k} - \frac{1}{\dot{a}} j_k \right) \delta\mu_{,k} dV - \sum_e \int_{\Omega^e} \left(-\dot{a}\frac{\partial c}{\partial x_1} + \frac{\partial j_k}{\partial x_k} \right) \tau^e \delta\mu_{,1} dV = \int_{S_0} \left(cn_1 + \frac{i}{\dot{a}} \right) \delta\mu dS.$$ (5.16)

Correspondingly, the components of the stiffness matrix should be updated as follows:

$$K_i^{\mu u,mn} = \frac{1}{\Omega} \left(\int_{V_0} B_1^{\mu,m} B_i^{u,n} dV - \int_{S_0} N^{\mu,m} B_i^{u,n} n_1 dS \right) + \frac{1}{\Omega} \int_{V_0} \tau^e \dot{a} B_1^{\mu,m} D_{1i}^{u,n} dV,$$ (5.17)
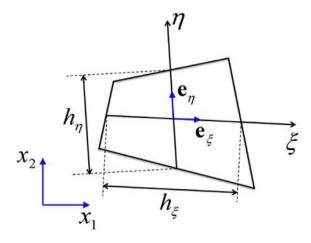
Fig. 2. Illustration of a 2D quadrilateral element for the SUPG method.
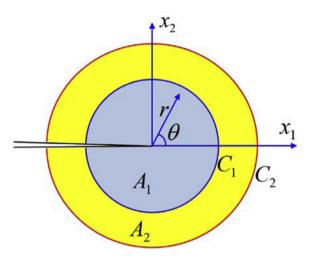

Fig. 3. Illustration of the domain integral method around a crack tip.

$$K^{\mu\mu,mn} = \frac{M_0}{\dot{a}}\left[\int_{V_0} B_i^{\mu,m}B_i^{\mu,n}dV + \int_{V_0}\tau^e\dot{a}B_1^{\mu,m}\left(D_{11}^{\mu,n} + D_{22}^{\mu,n}\right)dV\right], \tag{5.18}$$

where $D_{ij}^{u,n}$ and $D_{ij}^{\mu,n}$ are the second derivatives of the shape functions.

5.4. Domain integral method

To calculate the crack-tip energy release rate, the modified *J*-integral in Eq. (3.4) is calculated by the domain integral method. Similar to previous studies (Li et al., 1985; Bouklas et al., 2015a), the contour integral is converted to a domain integral as

$$J^* = -\int_{A_2}\left(\hat{\phi}\frac{\partial q}{\partial x_1} - \sigma_{ij}\frac{\partial u_i}{\partial x_1}\frac{\partial q}{\partial x_j}\right)dA + \int_{A_1+A_2}\frac{\partial \mu}{\partial x_1}(c - c_0)qdA, \tag{5.19}$$

where q is a sufficiently smooth function in A_2, varying from unity on the curve C_1 to zero on the curve C_2, and is set to be 1 in A_1, as illustrated in Fig. 3.

6. Numerical results and discussion

In this section we present numerical results obtained by the finite element method as described in Section 5 for the steady-state crack model in Fig. 1. We compare the numerical results with the analytical solution for the crack-tip fields as predicted in Section 4. We discuss the influence of the chemical boundary condition on the crack faces (immersed versus
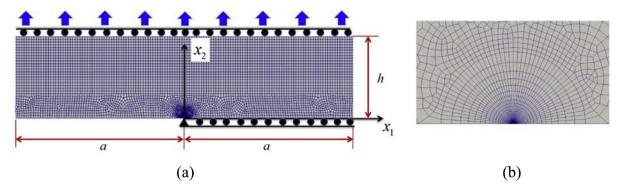
Fig. 4. (a) Finite element mesh for a half-strip model; (b) finite element mesh around a crack tip.

not-immersed). We examine the effects of crack speed on the crack-tip energy release rate and propose a method to measure intrinsic fracture toughness as a function of crack speed.

By symmetry, only half of the strip (Fig. 4(a)) is modeled with the finite element method. A constant displacement $u_2 = h\varepsilon_\infty$ is applied at the top of the strip ($x_2 = h$), where the traction is zero in the x_1 direction. The crack face ($x_1 < 0, x_2 = 0$) and the side faces of the strip ($x_1 = \pm a$) are all traction free. The symmetry condition is applied along the x_1 axis ahead of the crack tip ($x_1 > 0, x_2 = 0$). In the moving coordinate frame for the steady-state crack growth, the crack tip is fixed with zero displacement. Fig. 4(b) shows a typical finite element mesh around the crack tip, with concentric rings of elements up to a radius of $0.1h$ and increasingly finer mesh towards the crack tip. The quadrilateral 8u4p Taylor–Hood elements are used everywhere except for the first ring around the crack tip, where collapsed quarter-point Taylor–Hood elements (6u3p) are used, similar to that in a previous study (Bouklas et al., 2015a) for a stationary sharp crack. Plane strain conditions are assumed in the two-dimensional model.

To simulate a semi-infinite crack in an infinitely long strip, the half-strip model must be sufficiently long so that the inhomogeneous fields around the crack tip have no effect on the homogeneous states at both ends ($x_1 = \pm a$). This requires that $a >> h$ and $a >> l_{SS}$, where the steady-state diffusion length depends on the crack speed as defined by Eq. (3.2): $l_{SS} = D^*/\dot{a}$. In the finite element model, we use $a \geq 10\max(h, l_{SS})$ for all cases. As a result, the gel at the left end ($x_1 = -a$) is fully unloaded with the chemical potential of solvent equal to the initial value, i.e., $\mu_{-\infty} = 0$. At the right end ($x_1 = a$), the gel is stretched in the x_2 direction with the strain ε_∞ but stress free in the x_1 direction ($\sigma_{11} = 0$). Since the gel is not in direct contact with the external solution ahead of the crack tip, the solvent concentration remains constant at the right end and the gel behaves as an incompressible elastic solid ($\nu_\infty = 0.5$). Thus, under plane strain condition, we have $\varepsilon_{22} = \varepsilon_\infty$ and $\varepsilon_{11} = -\varepsilon_\infty$. Then, by Eq. (2.4), we obtain $\mu_\infty = -2G\Omega\varepsilon_\infty$ and $\sigma_{22} = 4G\varepsilon_\infty$. The chemical boundary conditions with $\mu_{-\infty} = 0$ and $\mu_\infty = -2G\Omega\varepsilon_\infty$ are imposed on the side faces ($x_1 = \pm a$) of the half strip model. At the top face, zero normal flux is assumed for solvent diffusion, i.e., $j_2 = 0$ at $x_2 = h$. For a mode-I crack, the symmetry dictates that the flux of solvent diffusion must be zero in the x_2 direction along the x_1 axis ahead of the crack tip, i.e., $j_2 = 0$ at ($x_1 > 0, x_2 = 0$). Along the crack face ($x_1 < 0, x_2 = 0$), the chemical potential is set to be zero for the immersed case whereas the normal flux is zero ($j_2 = 0$) for the not-immersed case.

In the finite element model, all the lengths are normalized by the strip thickness ($h = 1$). The crack speed is normalized as $\dot{a}h/D^*$, which is the Péclet number. The stress is normalized by the shear modulus G and the chemical potential by ΩG, whereas the normalized solvent concentration is Ωc. Within the linear poroelastic formulation, the elastic moduli (G and ν) are related to the gel properties by Eqs. (2.5) and (2.6). Taking $N\Omega = 0.001$ and $\chi = 0.2$ for the gel, we obtain by Eq. (2.1) $\lambda_0 = 3.215$ as the initial swelling ratio for $\mu_0 = 0$, and the corresponding Poisson's ratio is 0.2414 by Eq. (2.6). Poisson's ratio can be varied by using different values of $N\Omega$ and χ (Bouklas and Huang, 2012).

6.1. Poroelastic crack-tip fields

The asymptotic crack-tip fields are derived in Section 4 for steady-state crack growth in both the immersed and not-immersed cases. In particular, the stress and solvent concentration are singular as given by Eqs. (4.21) and (4.20), respectively. For the linearly poroelastic half-strip model, dimensional considerations suggest that the stress intensity factor and the T-stress take the form:

$$K_I = \zeta\left(\frac{\dot{a}h}{D^*}, \nu\right)G\varepsilon_\infty\sqrt{h}, \tag{6.1}$$

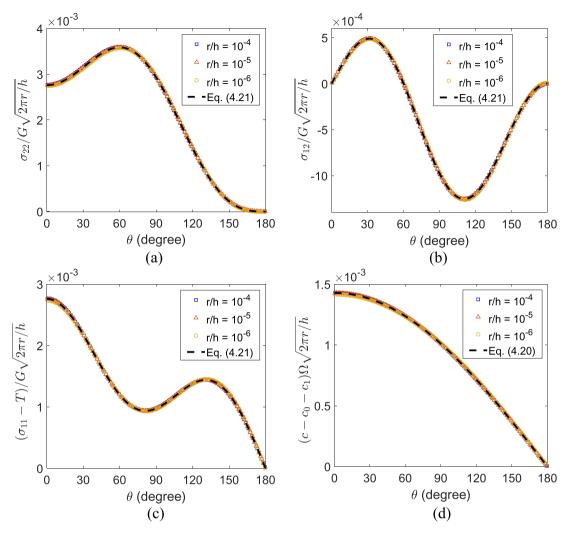$$T = \gamma\left(\frac{\dot{a}h}{D^*}, \nu\right)G\varepsilon_\infty, \tag{6.2}$$

Fig. 5. Numerical results for the angular distributions of the stress (a–c) and solvent concentration (d) around the crack tip ($\varepsilon_\infty = 0.001$), in comparison with the asymptotic analysis, for the immersed case with $\dot{a}h/D^* = 10$ and $\nu = 0.2414$.

where the dimensionless functions, $\zeta(\frac{\dot{a}h}{D^*}, \nu)$ and $\gamma(\frac{\dot{a}h}{D^*}, \nu)$, have to be determined numerically. For the immersed case, the T-stress is related to the constant term (Ωc_1) for solvent concentration by Eq. (4.25). The two parameters are independent for the not-immersed case, where Ωc_1 is to be determined numerically as well.

Fig. 5 shows the numerical results for the immersed case with $\dot{a}h/D^* = 10$ and $\nu = 0.2414$, comparing the angular distributions of the stress and solvent concentration with the asymptotic predictions. A small strain, $\varepsilon_\infty = 0.001$, is applied for the numerical calculation, but the normalized results are independent of the strain for the linear theory. A stress intensity factor, $K_I = 2.76 G \varepsilon_\infty \sqrt{h}$, is obtained by fitting the angular distribution of the stress component σ_{22} in Fig. 5(a) (or σ_{12} in Fig. 5(b)). Then, the T-stress, $T = -1.82 G \varepsilon_\infty$, can be obtained by fitting of σ_{11} in Fig. 5(c). Correspondingly, by Eq. (4.25), we obtain $\Omega c_1 = -0.47 \varepsilon_\infty$, with which the predicted angular distribution of the solvent concentration is in excellent agreement with the numerical result (Fig. 5(d)). The numerical results at different radii (close to the crack tip) are plotted to show that the angular distributions are independent of the radius as predicted for the singular crack-tip fields. The agreement confirms the square-root singularity for both the stress and concentration fields.

Similar numerical results are obtained for the not-immersed case with $\dot{a}h/D^* = 10$ and $\nu = 0.2414$, for which the stress intensity factor is found to be slightly smaller: $K_I = 2.67 G \varepsilon_\infty \sqrt{h}$. In this case, the T-stress and Ωc_1 are obtained independently by fitting the stress component σ_{11} and the solvent concentration: $T = -2.04 G \varepsilon_\infty$ and $\Omega c_1 = -0.214 \varepsilon_\infty$.

Fig. 6 shows the angular distributions of the chemical potential for the immersed and not-immersed cases. As predicted by Eq. (4.26), the leading term of the chemical potential for the immersed case is proportional to $\sqrt{r}$. With $K_I = 2.76 G \varepsilon_\infty \sqrt{h}$, we obtain $\kappa = 2.37$ by fitting the numerical results with the analytical prediction (Fig. 6(a)). For the not-immersed case, Eq. (4.36) predicts a constant term as the leading term, which is related to the T-stress and c_1 by Eq. (4.37). With $T = -2.04 G \varepsilon_\infty$ and $\Omega c_1 = -0.214 \varepsilon_\infty$ for this case, we obtain $\mu_{tip} = 0.604 G \Omega \varepsilon_\infty$ (as opposed to $\mu_{tip} = 0$ for the immersed case).
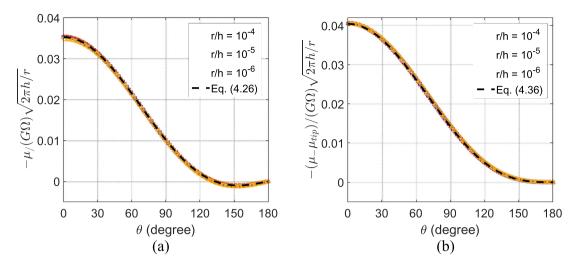
Fig. 6. Angular distributions of the chemical potential for the immersed (a) and not-immersed (b) cases ($\varepsilon_\infty = 0.001$, $\dot{a}h/D^* = 10$ and $\nu = 0.2414$).

By subtracting the constant μ_{tip}, the angular distribution of the chemical potential is again in close agreement with the analytical prediction with $K_I = 2.67G\varepsilon_\infty\sqrt{h}$ and $\kappa = 3$ (no additional fitting parameter) for the not-immersed case (Fig. 6(b)). Note that the slope of the chemical potential is zero at $\theta = \pi$ for the not-immersed case as required by the zero-flux condition at the crack face, whereas the slope is not zero for the immersed case, indicating solvent flux across the crack face. Again, the numerical results at different radii (close to the crack tip) are plotted to show that the angular distributions are independent of the radius as predicted.

For either immersed or not-immersed cases, there are three independent parameters for the poroelastic crack-tip fields (including K_I, T and κ or Ωc_1). As illustrated in Figs. 5 and 6, these crack-tip parameters can be determined by comparing the numerical results for the angular distributions of stress, solvent concentration and chemical potential to the analytical predictions. Alternatively, we may determine these parameters from the radial distributions of the displacement and chemical potential along the crack face. First, the stress intensity factor can be determined by the crack-opening displacement, comparing the numerical results with Eq. (4.30) as shown in Fig. 7(a). Next, to determine the T-stress, we note that $\sigma_{11} = T$ for $\theta = \pm\pi$ and $r \to 0$. By Eq. (2.4) the stress on the crack face ($\theta = \pm\pi$ and $r \to 0$) is related to the displacement and chemical potential as

$$\sigma_{11} = \frac{2G}{1-\nu}\frac{du_1}{dx_1} + \frac{2\nu - 1}{1-\nu}\frac{\mu_{tip}}{\Omega}. \tag{6.3}$$

For the immersed case, $\mu_{tip} = 0$ and the T-stress can be determined from the slope of the displacement u_1 along the crack face (Fig. 7(b)). For the not-immersed case, by plotting the chemical potential on the crack face as in Fig. 7(c), the constant μ_{tip} can be determined as the asymptote ($r \to 0$), with which the T-stress can be determined by Eq. (6.3). Then, with the T-stress and μ_{tip}, Ωc_1 can be determined by Eq. (4.37). Finally, the parameter κ for the immersed case can be determined by comparing the chemical potential straight ahead of the crack tip (i.e., $\theta = 0$) with Eq. (4.26) as shown in Fig. 7(d). Note that, in Fig. 7(a) and (d), the displacement and chemical potential of the first node ahead of the crack tip are ignored for the fitting, because numerical errors are typically expected for the first ring of elements around the crack tip.

Fig. 8 shows the normalized crack-tip parameters versus the normalized crack speed (the Péclet number, $Pe = \dot{a}h/D^*$) for $\nu = 0.2414$. The crack-tip parameters determined from the angular distributions and the radial distributions are nearly identical for each case. Fig. 8(a) shows that the stress intensity factors for both the immersed and not-immersed cases are smaller than the elastic case in Eq. (3.7), $K_e = 4G\varepsilon_\infty\sqrt{h}$. Remarkably, the stress intensity factor depends on the normalized crack speed non-monotonically (Fig. 8(a)), with a peak at $Pe \sim 10$ for the immersed case and at $Pe \sim 1$ for the not-immersed case. As the Péclet number increases or decreases, the stress intensity factor appears to approach the same limit for both the immersed and not-immersed cases. On the other hand, the magnitude of the T-stress increases monotonically with the Péclet number for the not-immersed case (Fig. 8(b)). The presence of a negative T-stress implies that the crack growth is directionally stable (Fleck et al., 1991; Chen and Dillard, 2001); a positive T-stress may be induced by stretching the strip in the x_1 direction, which could lead to a wavy crack path. For the immersed case, the parameter κ for the chemical potential in Eq. (4.26) also depends on the normalized crack speed non-monotonically (Fig. 8(c)), approaching the same limit ($\kappa \to 3$) as the Péclet number increases or decreases. For the not-immersed case, the chemical potential at the crack tip (μ_{tip}) is nearly zero for $Pe \ll 1$ (slow crack limit) but increases with increasing Péclet number (Fig. 8(d)).
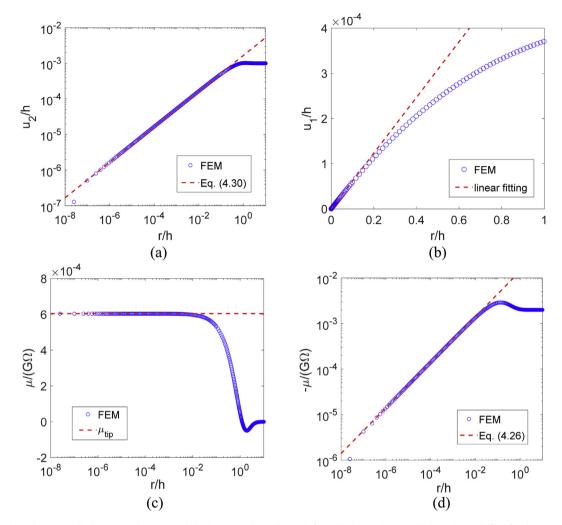
Fig. 7. (a) Crack opening displacement; (b) tangential displacement along the crack face; (c) chemical potential along the crack face for the not-immersed case; (d) chemical potential straight ahead of the crack tip for the immersed case ($\varepsilon_\infty = 0.001$, $\dot{a}h/D^* = 10$ and $\nu = 0.2414$).

6.2. Transition fields

The distributions of the stress components (σ_{22} and σ_{11}), solvent concentration, and chemical potential from the full-field numerical results for the immersed case with $\dot{a}h/D^* = 10$ and $\nu = 0.2414$ are shown in Fig. 9. Far away from the crack tip, all fields are homogeneous. The transition from the inhomogeneous, poroelastic crack-tip field to the homogeneous far-field solution is clearly shown in Fig. 7(d), where the chemical potential ahead of the crack tip follows the poroelastic crack-tip solution ($\mu \sim r^{1/2}$) up to a distance approximately equal to the steady-state diffusion length l_{SS} and becomes a constant ($\mu_\infty = -2G\Omega\varepsilon_\infty$) for $r > h$ as expected for the homogeneous far field. Since $h > l_{SS}$ in this case, there exists a transition field between the poroelastic crack-tip field and the far field. As noted in a previous study (Noselli et al., 2016), at a distance away from the crack tip (roughly $r > l_{SS}$), the solvent concentration remains a constant $c = c_0$, and $\mu \sim r^{-1/2}$ is predicted by the elastic crack-tip solution (incompressible with $\nu_\infty = 0.5$). Hence, for $h > l_{SS}$, the poroelastic crack-tip field first transitions to the elastic crack-tip field and then to the homogeneous far field, as shown in Fig. 10(a) for different h/l_{SS} ratios (or Péclet numbers). For each case with $h > l_{SS}$ ($Pe > 1$), the elastic crack-tip field is characterized by an elastic stress intensity factor, which may be determined by comparing to the elastic crack-tip solution (Noselli et al., 2016) for the chemical potential:

$$\mu = -\frac{\Omega K_e}{\sqrt{2\pi r}} \cos \frac{\theta}{2}. \tag{6.4}$$

It is found that the elastic stress intensity factor thus determined is identical to that for a linearly elastic strip as given in Eq. (3.7) and is independent of the crack speed. According to Eqs. (4.26) and (6.4), the chemical potential is re-scaled in Fig. 10(b), where the numerical results nearly collapse onto one curve except for the homogeneous far field. Apparently, while the stress intensity factor for the poroelastic crack-tip field ($r < l_{SS}$) varies slightly with the Péclet number, the stress
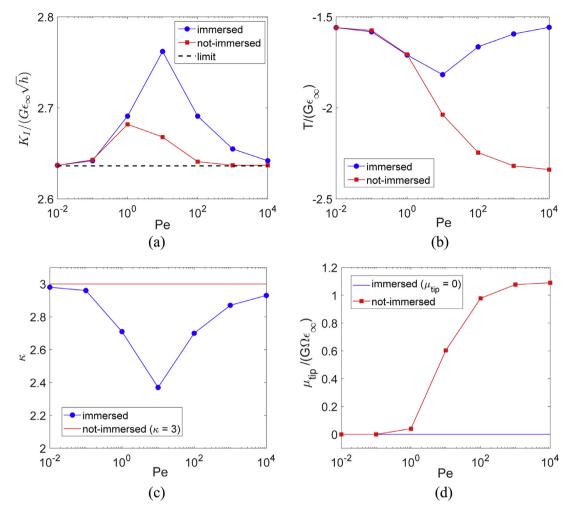
Fig. 8. Numerically determined crack-tip parameters versus the Péclet number ($Pe = \dot{a}h/D^*$): (a) normalized stress intensity factor; (b) normalized T-stress; (c) κ parameter for chemical potential; (d) normalized chemical potential at the crack tip.

intensity factor for the elastic crack-tip field ($l_{SS} < r < h$) is independent of the Péclet number. Interestingly, for a relatively large Péclet number ($Pe >> 1$), the poroelastic crack-tip solution intersects with the elastic crack-tip solution almost exactly at $r = l_{SS}$. As a result, the two stress intensity factors can be related approximately as:

$$K_I = \frac{K_e}{2(1 - \nu)}, \tag{6.5}$$

where we take $\kappa \approx 3$ for the immersed case. As shown in Fig. 8(c), $\kappa \to 3$ when $Pe >> 1$ for the immersed case. In general, for $\nu < 0.5$, we have $K_I < K_e$ and thus the stress intensity factor at the crack tip is reduced by the poroelastic shielding. The relation (6.5) is confirmed numerically by a crack-tip model for the fast crack limit with $Pe >> 1$ (see Appendix A). A similar relation was predicted by Hui et al. (2013) for a stationary crack at the short time limit.

The transition from the poroelastic crack-tip field to the elastic crack-tip field can also been seen in the opening stress ahead of the crack tip (Fig. 10(c)). While the square-root singularity is predicted for the stress in both the crack-tip fields, the stress intensity factors are different ($K_I < K_e$) and thus the stress near the crack tip is reduced by the poroelastic effect. On the other hand, such transition appears to be absent in the crack-opening displacement (Fig. 10(d)). Apparently, with the relation in Eq. (6.5) for the two stress intensity factors, the leading term for the crack opening displacement as predicted by Eq. (4.30) for the poroelastic crack-tip field is identical to that for the elastic crack-tip field (with $\nu_\infty = 0.5$). Therefore, the two crack-tip fields are indistinguishable in the crack opening displacement, which is another observation supporting the relation in Eq. (6.5).

It is further noted that the elastic crack-tip solution for the chemical potential in Eq. (6.4) does not satisfy the zero-flux condition on the crack faces. Thus, it appears that the elastic crack-tip field does not exist theoretically for the not-immersed case. However, similar transitions are observed in our numerical results in the not-immersed cases, as shown in Fig. 11 for
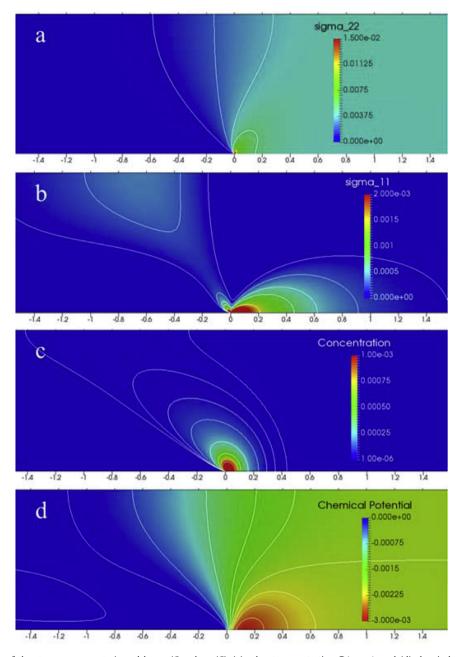
Fig. 9. Distributions of the stress components (a and b: σ_{22}/G and σ_{11}/G), (c) solvent concentration $\Omega(c - c_0)$, and (d) chemical potential $\mu/(\Omega G)$ in a half-strip model with $\dot{a}h/D^* = 10$ and $\nu = 0.2414$.

the chemical potential and opening stress ahead of the crack tip. It may be expected that the angular distribution of the chemical potential is different from Eq. (6.4) for the transition field in the not-immersed case.

When $h < l_{SS}$, the elastic crack-tip field does not exist even for the immersed case and a different transition from the poroelastic crack-tip field to the homogeneous far field is observed in Fig. 12. In this case, the chemical potential follows the poroelastic crack-tip solution up to approximately $x_1 = h$ and becomes a constant for $x_1 > l_{SS}$. In between ($h < x_1 < l_{SS}$), the magnitude of the chemical potential increases almost linearly (i.e., $\mu \sim r$). It is found that such a transition can be predicted by a one-dimensional (1D) diffusion model for both the immersed and not-immersed cases at the slow crack limit with $Pe < < 1$ (see Appendix B). As shown in Fig. 12, both the chemical potential and the opening stress ahead of the crack tip ($x_1 > h$) are well predicted by the 1D model for the case with $Pe = 0.01$.
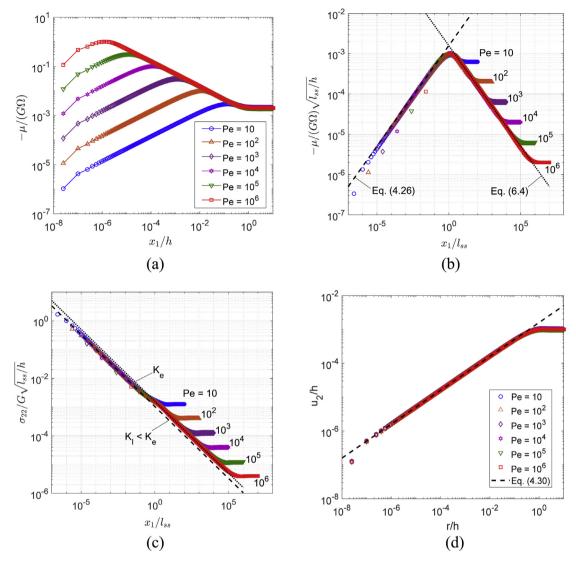
Fig. 10. (a and b) Chemical potential straight ahead of the crack tip for different Péclet numbers ($Pe > 1$); (c) opening stress straight ahead of the crack tip; (d) crack-opening displacement, all for immersed cases with $\nu = 0.2414$.

6.3. Energy release rate

In a poroelastic material, the change of stored elastic energy associated with crack growth includes two parts: the energy dissipation due to solvent diffusion around the crack tip and the elastic energy released by fracture. In Eq. (3.4), the contour integral (J_Γ in Eq. (4.33)) is essentially the classical J-integral that calculates the energy change within the contour, whereas the domain integral (J_A in Eq. (4.34)) calculates the dissipated energy by diffusion. The modified J-integral ($J^* = J_\Gamma + J_A$) is thus the fracture energy release rate (per unit area of crack growth), which is independent of the contour path. For the long strip model under the plane-strain condition, the remotely applied energy release rate is given by Eq. (3.6), which is independent of the crack speed as in the case of an elastic strip. By the modified J-integral, we calculate the crack-tip energy release rate ($J_{tip} = J^*$) for a poroelastic strip, which may depend on the crack speed through the length scale l_{SS}. Dimensional consideration suggests that

$$\frac{J^*}{J_e} = \Lambda\left(\frac{\dot{a}h}{D^*}, \nu\right),\tag{6.6}$$

where $J_e = 4G\varepsilon_\infty^2 h$ and the dimensionless function $\Lambda(\frac{\dot{a}h}{D^*}, \nu)$ is to be determined numerically.

Fig. 13 shows the path-independence of the modified J-integral (J^*), in comparison with the classical J-integral (J_Γ), both calculated by the domain integral method. As the contour radius varies from $10^{-7}h$ to $10^{-1}h$, the modified J-integral remains

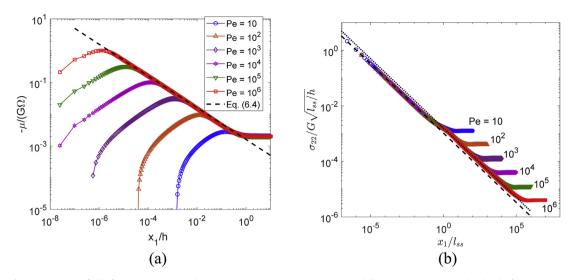**Fig. 11.** Transition fields for the not-immersed cases ($Pe > 1$): (a) chemical potential and (b) opening stress, straight ahead of the crack tip.
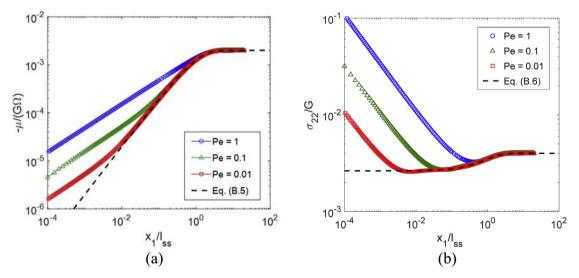

Fig. 12. (a) Chemical potential and (b) opening stress, straight ahead of the crack tip for $Pe \leq 1$. The predictions by the 1D model are shown as dashed lines for comparison.

a constant except for the contour closest to the crack tip where the J-integral is slightly lower due to limited numerical accuracy at the crack tip. On the other hand, the classical J-integral shows clear dependence on the contour radius, approaching the modified J-integral ($J_\Gamma \to J^*$) as the contour radius decreases but approaching the remotely applied energy release rate ($J_\Gamma \to J_e$) as the contour radius increases. When taking a contour close to the crack tip ($r \to 0$), as the domain integral approaches zero ($J_A \to 0$), the contour integral approaches the crack-tip energy release rate. On the other hand, taking a contour far away from the crack tip, the applied energy release rate is obtained by the contour integral as long as the solvent diffusion zone is fully enclosed within the contour. The path dependence of the classical J-integral is a direct consequence of solvent diffusion around the crack tip.

It is interesting to note that the solvent diffusion zone around the crack tip typically extends beyond the region of the poroelastic crack-tip field ($r < l_{SS}$). For $h > l_{SS}$, within the transition region (roughly $l_{SS} < r < h$), the chemical potential is inhomogeneous ($\mu \sim r^{-1/2}$) and hence solvent diffusion occurs, but the divergence of solvent flux is zero so that the solvent concentration remains homogeneous. Therefore, while the stress and chemical potential in the transition region follows the elastic crack-tip solution, there is actually energy dissipation due to solvent diffusion in this region. As shown in Fig. 13, the classical J-integral becomes path-independent only for $r/h > 10^{-2}$ while $l_{SS}/h = 10^{-3}$. Thus, the solvent diffusion zone extends up to $r \sim 10 l_{SS}$ although the poroelastic crack-tip field is valid only up to $r \sim l_{SS}$. On the other hand, when $h < l_{SS}$, Fig. 12 shows that the poroelastic crack-tip field is valid up to $r \sim h$ but the solvent diffusion zone extends up to $r \sim 10 l_{SS}$ (ahead of the crack tip).
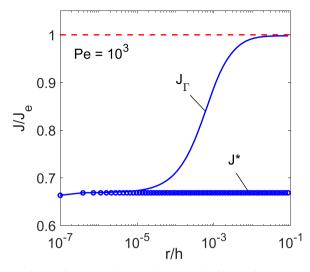
Fig. 13. Comparison of the modified J-integral (J^*) and the classical J-integral (J_Γ), calculated by the domain integral method with the contour radius from $10^{-7}h$ to $10^{-1}h$.
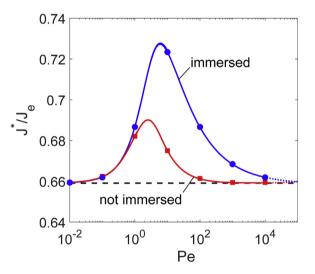

Fig. 14. Modified J-integral (J^*), normalized by the applied energy release rate (J_e), plotted as a function of the Péclet number ($Pe = \dot{a}h/D^*$) for the immersed and not-immersed cases ($\nu = 0.2414$).

With the modified J-integral and the domain integral method, the crack-tip energy release rate (J^*) for steady-state crack growth in a linearly poroelastic strip is calculated as a function of the normalized crack speed ($Pe = \dot{a}h/D^*$) for both the immersed and not-immersed cases with $\nu = 0.2414$, as shown in Fig. 14. Alternatively, the modified J-integral can also be calculated using Eq. (4.35) with the stress intensity factor in the poroelastic crack-tip field (Fig. 8(a)). As shown in Fig. 14 by the lines and symbols, the results from both calculations agree closely. Interestingly, J^*/J_e, the ratio between the crack-tip energy release rate and the applied energy release rate, depends on the normalized crack speed non-monotonically. For the immersed case, J^*/J_e is maximized at $Pe \sim 10$, with around 72% of the total energy released at the crack-tip and ~28% dissipated by solvent diffusion. The ratio J^*/J_e drops to around 66% at both limits for slow and fast crack growth. The two limiting cases are discussed further in the Appendices, with a crack-tip model for the fast crack limit ($Pe >> 1$) and a 1D model for the slow crack limit ($Pe << 1$). It is found that the ratio J^*/J_e is identical at both limits: $J^*/J_e \to \frac{1}{2(1-\nu)}$, shown as the horizontal dashed line in Fig. 14.

For the not-immersed case, the ratio J^*/J_e has a peak at $Pe \sim 3$, with around 69% of the total energy released at the crack tip. As noted earlier (Fig. 8(a)), the poroelastic stress intensity factor for the not-immersed case is lower than the immersed case. Correspondingly, the crack-tip energy release rate is lower as well. For very slow crack growth ($Pe < < 1$), J^*/J_e approaches the same limit as that for the immersed case. For very fast crack growth ($Pe > 10^4$), however, the calculated

J^*/J_e appears to approach the same limit as well.[3] Unlike the immersed case, the fast crack limit for the not-immersed case cannot be confirmed strictly by the crack-tip model (Appendix A) because the elastic solution in Eq. (6.4) does not satisfy the zero-flux condition along the crack face and hence cannot be imposed as the boundary condition for the crack-tip model. Nevertheless, our calculations of the modified J-integral and the stress intensity factor both suggest the same fast crack limit for the immersed and not-immersed cases.

6.4. Implications for experiments

As a hypothetical fracture criterion for gels, it is the crack-tip energy release rate ($J_{tip} = J^*$) that drives the crack growth. When the crack grows in a steady state, the crack-tip energy release rate equals the intrinsic fracture toughness of the gel, which may or may not depend on the crack speed. The intrinsic fracture toughness as a function of crack speed may be determined experimentally as follows. Subject to an applied strain ε_∞, if the steady-state crack speed $\dot{a}$ can be measured in a long strip specimen, the intrinsic fracture toughness corresponding to the crack speed can be determined as

$$\Gamma = J^* = 4G\varepsilon_\infty^2 h\Lambda\left(\frac{\dot{a}h}{D^*}, \nu\right), \tag{6.7}$$

where the dimensionless function $\Lambda(\frac{\dot{a}h}{D^*}, \nu)$ can be calculated as shown in Fig. 14. The poroelastic properties (G, ν and D^*) of the material must be determined separately by independent measurements, e.g., indentation relaxation tests (Hu et al., 2011). On the other hand, the remotely applied energy release rate ($J_e = 4G\varepsilon_\infty^2 h$) is often taken as the apparent fracture toughness (Long and Hui, 2016), which is generally higher than the intrinsic fracture toughness. We note that, while linear poroelasticity and plane strain conditions are assumed in the present study, Eq. (6.7) may be generalized to nonlinear poroelasticity as well as other loading conditions such as plane stress, although the specific form would be different for the applied energy release rate (J_e) and the dimensionless function $\Lambda(\frac{\dot{a}h}{D^*}, \nu)$.

Alternatively, if the intrinsic fracture toughness (Γ) is known for the gel, either as a function of crack speed or is independent of crack speed, Eq. (6.7) may be used to predict the steady-state crack speed in a long strip specimen subject to an applied strain ε_∞. In particular, if Γ is independent of the crack speed, there exist two critical strains: $\varepsilon_{c1} = \sqrt{\frac{\Gamma}{4Gh\Lambda_{max}}}$ and $\varepsilon_{c2} = \sqrt{\frac{\Gamma(1-\nu)}{2Gh}}$, where Λ_{max} is the peak value of the function $\Lambda(\frac{\dot{a}h}{D^*}, \nu)$ and depends on Poisson's ratio. If $\varepsilon_\infty < \varepsilon_{c1}$, $J^* < \Gamma$ for all crack speed and thus the crack will not grow at all; this suggests a threshold strain for crack growth in the gel. If $\varepsilon_\infty > \varepsilon_{c2}$, $J^* > \Gamma$ for all crack speed and thus no steady-state crack growth is predicted without considering inertial effects; this suggests a dynamic regime for crack growth under a large strain. If $\varepsilon_{c1} < \varepsilon_\infty < \varepsilon_{c2}$, quasi-static steady-state crack growth is predicted by setting $J^* = \Gamma$. Interestingly, the results in Fig. 14 predict two possible crack speeds, while one is stable and the other is unstable. The stability of the crack speed can be determined by a perturbation method: at a particular crack speed, we have $J^*(\dot{a}) = \Gamma$; with a slight perturbation to the crack speed, $\delta\dot{a}$, the energy release rate becomes $J^* + \delta J^*$, where $\delta J^* = \frac{d\Lambda}{d\dot{a}} J_e \delta\dot{a}$. If $\frac{d\Lambda}{d\dot{a}} > 0$, the change of the energy release rate would further increase the perturbation, and as a result the crack speed is unstable. On the other hand, if $\frac{d\Lambda}{d\dot{a}} < 0$, the crack speed is stable. Therefore, based on Fig. 14, for a particular $J^* = \Gamma$, the faster crack speed is stable and the slower speed is unstable. To predict the stable crack speed, we plot in Fig. 15 the Péclet number as the normalized crack speed (stable branch only) versus J_e/Γ as the normalized loading parameter. Notably, such a plot resembles the V-G curve for environmentally assisted subcritical crack growth in many brittle solids (Lawn, 1993), with a threshold energy release rate for crack initiation and a critical energy release rate for fast crack growth. Apparently, the kinetics of solvent diffusion leads to a similar effect on crack growth as diffusion of environmental species for subcritical cracking. However, unlike subcritical cracking, the threshold load in terms of the applied energy release rate J_e is greater than the intrinsic fracture toughness ($J_e > \Gamma$) for the steady-state crack growth in a poroelastic specimen, hence a "supercritical" behavior as a result of poroelastic toughening.

Baumberger et al. (2006) reported an experimental study of crack growth in gelatin gels. Their experimental results are qualitatively consistent with the numerical calculations in the present study despite the limitation of linear poroelasticity. First, "velocity toughening" was noted in their experiments, as the applied energy release rate (J_e) increased with increasing crack velocity, consistent with the stable branch in Fig. 15 assuming a constant intrinsic fracture toughness (Γ). However, quantitatively, the "velocity toughening" by linear poroelasticity as discussed in the present study is not sufficient to explain the rate dependence of toughness in the experiments. The intrinsic toughness itself could be rate dependent as discussed by Baumberger et al. (2006). Second, they found that increasing solvent viscosity slowed down the crack growth. By the theory of linear poroelasticity, the solvent viscosity can be related to the cooperative diffusivity as (Bouklas and Huang, 2012):

$$D^* = \frac{2(1-\nu)}{1-2\nu}\frac{Gk}{\eta}, \tag{6.8}$$

where η is the solvent viscosity and k is permeability of the gel network. Thus, increasing the solvent viscosity would decrease the cooperative diffusivity, which in turn would decrease the crack speed to maintain the same Péclet number

---

[3] As the Péclet number increases, an increasingly finer mesh is required at the crack tip to achieve sufficient accuracy in the calculation of the modified J-integral. With the crack-tip element size as small as $10^{-7}h$, the calculation is numerically converged for Péclet numbers up to 10^4, beyond which numerical error becomes significant ($> 1\%$).
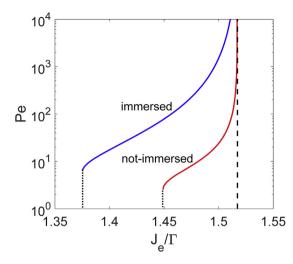
Fig. 15. Normalized crack speed (the Péclet number) as a function of the normalized loading parameter for a poroelastic strip specimen.

($Pe = \dot{a}h/D^*$) under the same loading condition. Third, they found soaking the crack tip with solvent increased the crack velocity. When the applied total energy release rate was too low for the "dry" crack to grow, the "soaked" crack would still grow. The "soaking" effect may be qualitatively understood by comparing the immersed and not-immersed cases in Fig. 15. Under the same applied load (J_e/Γ), the Péclet number for the immersed case ("soaked") is larger than the not-immersed case ("dry") and hence the "soaked" crack grows faster. Moreover, since the critical load ($J_e = \Gamma/\Lambda_{\max}$) for the immersed case is lower than the not-immersed case, the "soaked" crack can grow at a lower J_e than the "dry" crack, consistent with the experiments. While the qualitative agreement is encouraging, quantitative modeling of crack growth in gels would in general require a nonlinear large deformation formulation, which is left for future studies.

7. Summary

The main results of the present study are summarized as follows.

- Based on a linear poroelastic formulation, an asymptotic analysis of the poroelastic crack tip fields is developed for steady-state crack growth in polymer gels. Numerically confirmed, the asymptotic analysis predicts singular stress and solvent concentration fields with a poroelastic stress intensity factor as well as the leading non-singular terms for the chemical potential. Moreover, the poroelastic stress intensity factor is related to the modified J-integral as the crack-tip energy release rate.
- A linear poroelastic finite element method is developed using Taylor–Hood elements and the consistent streamline-upwind-Petrov–Galerkin (SUPG) method for numerical stabilization.
- For a semi-infinite crack in a long strip specimen subject to plane-strain loading, the poroelastic stress intensity factor is calculated as function of crack speed, which is generally smaller than the stress intensity factor predicted by linear elasticity due to solvent diffusion (poroelastic shielding). Similarly, the crack-tip energy release rate is smaller than the applied energy release rate as a result of energy dissipation associated with solvent diffusion.
- The effect of crack speed on the poroelastic stress intensity factor and the crack-tip energy release rate is captured by the dimensionless Péclet number ($Pe = \dot{a}h/D^*$), where the cooperative diffusivity D^* is related to the swelling ratio of the gel (or solvent content) as well as its intrinsic properties (e.g., Nk_BT, χ and D). It can also be related to solvent viscosity and permeability.
- For relatively fast crack growth ($Pe > 1$), the size of the poroelastic crack-tip field (or K-field) is characterized by a diffusion length scale that is inversely proportional to the crack speed ($l_{SS} = D^*/\dot{a}$). In this case, the poroelastic K-field transitions to an elastic K-field at a distance proportional to the diffusion length, and the modified J-integral decreases with increasing crack speed, approaching a limit for $Pe >> 1$ (the fast crack limit).
- For relatively slow crack growth ($Pe < 1$), the poroelastic crack-tip field is confined by the strip thickness and transitions to a one-dimensional diffusion zone ahead of the crack tip. In this case, the modified J-integral decreases with decreasing crack speed, approaching a limit for $Pe << 1$ (the slow crack limit).
- With the same values at the fast and slow crack limits, the crack-tip energy release rate (normalized by the applied energy release rate) depends on the Péclet number non-monotonically, with a peak at $Pe = 1 \sim 10$.
- Both immersed and not-immersed crack face conditions are considered. Under the same loading conditions, the poroelastic stress intensity factor and the modified J-integral are generally higher for the immersed case than not-immersed, but they approach the same values at the fast and slow crack limits.
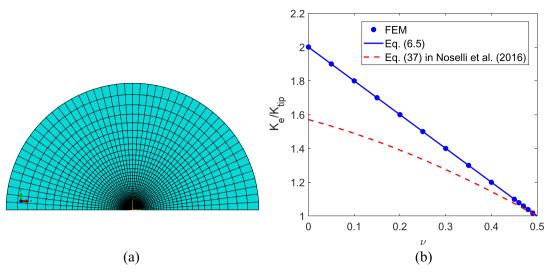
Fig. 16. (a) Finite element mesh for the crack-tip model; (b) effect of Poisson's ratio on the stress intensity factor, comparing the numerical results with analytical predictions.

- By measuring crack speed under a remote loading condition, the intrinsic fracture toughness of the gel may be determined by calculating the modified *J*-integral as a fraction of the applied energy release rate, depending on the Péclet number and Poisson's ratio.
- If the intrinsic fracture toughness of the gel is independent of crack speed, the apparent fracture toughness including the energy dissipation due to solvent diffusion would be generally greater than the intrinsic toughness (i.e., poroelastic toughening) and depends on the crack speed. For a long strip specimen, quasi-static steady-state crack growth is predicted when the applied strain is between two critical strains, with increasing crack speed for increasing strain.
- The present theoretical and numerical results are qualitatively consistent with the experiments by Baumberger et al. (2006) for crack growth in gelatin gels, with the effects of solvent viscosity and crack-tip soaking as well as the apparent "velocity roughening".
- Finally, in comparison to Noselli et al. (2016): (1) the present work develops a similar asymptotic solution of the poroelastic crack-tip fields for the immersed case, but with additional terms for the *T*-stress and solvent concentration; (2) while not considered in the previous work, the asymptotic solution for the not-immersed case is also developed in the present study; (3) numerically, a long-strip specimen with a finite thickness is considered here, while the previous work assumed infinite thickness as in the crack-tip model (Appendix A); (4) a cohesive zone model was proposed in the previous work that led to rate-dependent poroelastic toughening, whereas the present study predicts a rate dependence resulting from the finite specimen size.

Acknowledgments

Appendix A. A steady-state crack-tip model for $h >> l_{SS}$ ($Pe >> 1$)

The full-field half-strip model becomes numerically challenging when the two length scales (h and l_{SS}) are dramatically different. When $h >> l_{SS}$ (small-scale diffusion), the finite element mesh near the crack tip must be sufficiently fine to resolve the diffusion length l_{SS}. Alternatively, a crack-tip model may be constructed for such a case, where the elastic crack-tip solution can be used as the boundary condition similar to that in Noselli et al. (2016). We note that such an approach is possible only for the immersed case, when there exists an elastic crack-tip solution as the transition field between the poroelastic crack-tip field ($r < l_{SS}$) and the homogeneous far field ($r > h$).

Fig. 16(a) shows the finite element mesh for the crack-tip model. Here, the only relevant length scale is the steady-state diffusion length l_{SS}, which can be set to 1 after normalization. The circular outer boundary at $r = n l_{SS}$ is chosen to be in the region of the elastic transition field with $1 < n < h/l_{SS}$. To fully account for the energy dissipation due to solvent diffusion in the transition region, n should be sufficiently large so that energy dissipation due to solvent diffusion is negligible beyond the outer boundary. As a result, the classical *J*-integral along the outer boundary is essentially the same as the applied energy release rate as given in Eq. (3.6). A reasonable choice is to take $n > 10$. The traction boundary condition is then set by the elastic crack-tip solution with a stress intensity factor K_e as given in Eq. (3.7). Similarly, the chemical potential at

the outer boundary can be set by Eq. (6.4). After normalization, the boundary condition becomes proportional to $\sqrt{h/l_{SS}}$. Consequently, the numerical results for the stress field in the crack-tip model are linearly proportional to $\sqrt{h/l_{SS}}$, and so is the normalized stress intensity factor in the poroelastic crack-tip field, i.e., $\bar{K}_{tip} \sim \sqrt{h/l_{SS}}$. Accordingly, the dimensional stress intensity factor ($K_{tip} = \bar{K}_{tip} G \sqrt{l_{SS}}$) is independent of l_{SS} or the crack speed. Hence, for $Pe > > 1$, the crack-tip model predicts that $K_{tip} = \zeta_\infty(\nu) G \varepsilon_\infty \sqrt{h}$, where the effect of Poisson's ratio is found to follow Eq. (6.5) as shown in Fig. 16(b).

Similar results were reported by Noselli et al. (2016), where the stress intensity factor was found to be independent of the crack speed (unless a cohesive zone is assumed ahead of the crack tip), assuming small-scale diffusion ($h > > l_{SS}$). They suggested a different relation for the elastic and poroelastic stress intensity factors, which however does not agree with our numerical results (see Fig. 16(b)).

Calculation of the modified J-integral confirms the relationship in Eq. (4.35) and hence, for $Pe > > 1$, the crack-tip energy release rate is independent of the crack speed but depends on Poisson's ratio as follows:

$$J^* = \frac{2G\varepsilon_\infty^2 h}{1-\nu} = \frac{J_e}{2(1-\nu)}. \tag{A.1}$$

In general, with $\nu < 0.5$, $J^* < J_e$ due to energy dissipation by solvent diffusion around the crack tip, referred to as poroelastic toughening by Noselli et al. (2016).

Appendix B. A one-dimensional diffusion model for $h < < l_{SS}$ ($Pe < < 1$)

When $h < < l_{SS}$, the aspect ratio (a/h) of the half-strip model must be very large in order to simulate a semi-infinite crack in an infinitely long strip, while the finite element mesh near the crack tip must be sufficiently fine to resolve the length h. In this case, the extent of the poroelastic crack-tip field is limited by the strip thickness h, beyond which the solvent diffusion is primarily one-dimensional in the x_1 direction. Thus, Eq. (3.1) becomes approximately

$$-\dot{a}\frac{\partial c}{\partial x_1} = D^* \frac{\partial^2 c}{\partial x_1^2}, \tag{B.1}$$

which can be solved by, for $x_1 > 0$

$$c(x_1) = c_0 + A \exp\left(-\frac{x_1}{l_{SS}}\right). \tag{B.2}$$

The mechanical equilibrium in this case requires that $\sigma_{11} = 0$. Hence, by Eq. (2.4)

$$2G\left[\varepsilon_{11} + \frac{\nu}{1-2\nu}\varepsilon_{kk}\right] - \frac{\mu - \mu_0}{\Omega} = 0. \tag{B.3}$$

Since $\varepsilon_{kk} = \Omega(c - c_0)$ and $\varepsilon_{22} = \varepsilon_\infty$ for $x_1 > 0$, we obtain the chemical potential ahead of the crack tip (plane strain) as:

$$\mu = \mu_0 + 2\Omega G\left[\frac{1-\nu}{1-2\nu}\Omega A \exp\left(-\frac{x_1}{l_{SS}}\right) - \varepsilon_\infty\right]. \tag{B.4}$$

Behind the crack tip ($x_1 < 0$), the field is nearly homogeneous with $\mu = \mu_0$ for both the immersed and not-immersed cases. Therefore, the coefficient A in (Eq. B.4) can be determined approximately by setting $\mu = \mu_0$ at $x_1 = 0$ as the continuity condition. The resulting chemical potential for $x_1 > 0$ is then obtained as

$$\mu = \mu_0 + \mu_\infty\left[1 - \exp\left(-\frac{x_1}{l_{SS}}\right)\right], \tag{B.5}$$

where $\mu_\infty = -2\Omega G\varepsilon_\infty$. The prediction by Eq. (B.5) compares closely with the numerical results for the cases with $h < l_{SS}$ in the region $x_1 > h$, as shown in Fig. 12(a).

By Eq. (2.4), the opening stress ahead of the crack tip is obtained as

$$\sigma_{22}(x_1) = 4G\varepsilon_\infty\left[1 - \frac{1-2\nu}{2(1-\nu)}\exp\left(-\frac{x_1}{l_{SS}}\right)\right], \tag{B.6}$$

which agrees with the numerical results in the region $x_1 > h$ for the cases with $h < l_{SS}$, as shown in Fig. 12(b). By (Eq. B.6), the opening stress is relaxed ahead of the crack tip due to the poroelastic effect, and the poroelastic relaxation decays exponentially with a characteristic length l_{SS}. In this case, the assumption of steady-state crack growth remains valid as long as the length of the specimen is infinite or much greater than the diffusion length ($a > > l_{SS}$).

With the 1D approximation, we calculate the domain integral in Eq. (3.4) as

$$J_A = \int_A (c - c_0)\frac{\partial \mu}{\partial x_1} dA \approx 2h \int_0^\infty (c - c_0)\frac{\partial \mu}{\partial x_1} dx_1 = -\frac{2(1-2\nu)}{1-\nu}G\varepsilon_\infty^2 h. \tag{B.7}$$

Meanwhile, the contour integral over a contour far away from the crack tip gives the applied energy release rate, i.e., $J_\Gamma = J_e = 4G\varepsilon_\infty^2 h$. Therefore, the crack-tip energy release rate by the modified J-integral for this case ($h < < l_{SS}$) is:

$$J^* = J_\Gamma + J_A = \frac{2G\varepsilon_\infty^2 h}{1-\nu} = \frac{J_e}{2(1-\nu)}, \tag{B.8}$$

which is identical to the result for $h > > l_{SS}$ (Eq. (A.1)). Incidentally, for different reasons, the ratio J^*/J_e approaches the same limit for both fast and slow crack growth in a linearly poroelastic long-strip specimen.

References

Atkinson, C., Craster, R.V., 1991. Plane strain fracture in poroelastic media. Proc. R. Soc. Lond. A 434, 605–633.
Balay, S., Abhyankar, S., Adams, M.F., Brown, J., Brune, P., Buschelman, K., Dalcin, L., Eijkhout, V., Gropp, W.D., Kaushik, D., Knepley, M.G., McInnes, L.C., Rupp, K., Smith, B.F., Zampini, S., Zhang, H., 2017. PETSc Users Manual. Argonne National Laboratory ANL-95/11 - Revision 3.8.
Baumberger, T., Caroli, C., Martina, D., 2006. Solvent control of crack dynamics in a reversible hydrogel. Nat. Mater. 5, 552–555.
Biot, M.A., 1941. General theory of three-dimensional consolidation. J. Appl. Phys. 12, 155–164.
Bonn, D., Kellay, H., Prochnow, M., Ben-Djemiaa, K., Meunier, J., 1998. Delayed fracture of an inhomogeneous soft solid. Science 280, 265–267.
Bouklas, N., Huang, R., 2012. Swelling kinetics of polymer gels: comparison of linear and nonlinear theories. Soft Matter 8, 8194–8203.
Bouklas, N., Landis, C.M., Huang, R., 2015a. Effect of solvent diffusion on crack-tip fields and driving force for fracture of hydrogels. J. Appl. Mech. 82, 081007.
Bouklas, N., Landis, C.M., Huang, R., 2015b. A nonlinear, transient finite element method for coupled solvent diffusion and large deformation of hydrogels. J. Mech. Phys. Solids 79, 21–43.
Brooks, A.N., Hughes, T.J.R., 1982. Streamline upwind Petrov–Galerkin formulations for convection dominated flows with particular emphasis on the incompressible Navier–Stokes equations. Comput. Meth. Appl. Mech. Eng. 32, 199–259.
Calvert, P., 2009. Hydrogels for soft machines. Adv. Mater. 21, 743–756.
Chen, B., Dillard, D.A., 2001. The effect of the T-stress on crack path selection in adhesively bonded joints. Int. J. Adhesion Adhesives 21, 357–368.
Drury, J.L., Mooney, D.J., 2003. Hydrogels for tissue engineering: scaffold design variables and applications. Biomaterials 24, 4337–4351.
Fleck, N.A., Hutchinson, J.W., Suo, Z., 1991. Crack path selection in a brittle adhesive layer. Int. J. Solids Struct. 27, 1683–1703.
Flory, P.J., 1953. Principles of Polymer Chemistry. Cornell University Press, Ithaca, NY.
Forte, A.E., D'Amico, F., Charalambides, M.N., Dini, D., Williams, J.G., 2015. Modelling and experimental characterisation of the rate dependent fracture properties of gelatine gels. Food Hydrocoll. 46, 180–190.
Franca, L.P., Frey, S.L., Hughes, T.J.R., 1992. Stabilized finite-element methods 1. Application to the advective-diffusive model. Comput. Meth. Appl. Mech. Eng 95, 253–276.
Franca, L.P., Hauke, G., Masud, A., 2006. Revisiting stabilized finite element methods for the advective–diffusive equation. Comput. Meth. Appl. Mech. Eng. 195, 1560–1572.
Gong, J.P., Katsuyama, Y., Kurokawa, Y., Osada, Y., 2003. Double-network hydrogels with extremely high mechanical strength. Adv. Mater. 15, 1155–1158.
Hong, W., Zhao, X., Zhou, J., Suo, Z., 2008. A theory of coupled diffusion and large deformation in polymeric gels. J. Mech. Phys. Solids 56, 1779–1793.
Hong, W., Liu, Z., Suo, Z., 2009. Inhomogeneous swelling of a gel in equilibrium with a solvent and mechanical load. Int. J. Solids Struct. 46, 3282–3289.
Hu, Y., Chen, X., Whitesides, G.M., Vlassak, J.J., Suo, Z., 2011. Indentation of polydimethylsiloxane submerged in organic solvents. J. Mater. Res. 26, 785.
Hui, C.-Y., Lin, Y.Y., Chuang, F.-C., Shull, K.R., Lin, W.-C., 2006. A contact mechanics method for characterizing the elastic properties and permeability of gels. J. Polym. Sci. Part B: Polym. Phys. 44, 359–370.
Hui, C.Y., Long, R., Ning, J., 2013. Stress relaxation near the tip of a stationary mode I crack in a poroelastic solid. J. Appl. Mech. 80, 021014.
Johnson, C., 1987. Numerical Solution of Partial Differential Equations by the Finite Element Method. Cambridge University Press.
Kang, M.K., Huang, R., 2010. A variational approach and finite element implementation for swelling of polymeric hydrogels under geometric constraints. J. Appl. Mech. 77, 061004.
Lawn, B., 1993. Fracture of Brittle Solids. Cambridge University Press.
Langer, R., 2006. Biomaterials for drug delivery and tissue engineering. MRS Bull 31, 477–485.
Lefranc, M., Bouchaud, E., 2014. Mode I fracture of a biopolymer gel: rate-dependent dissipation and large deformations disentangled. Extreme Mech. Lett. 1, 97–103.
Li, F.Z., Shih, C.F., Needleman, A., 1985. A comparison of methods for calculating energy-release rates. Eng. Fract. Mech. 21, 405–421.
Long, R., Hui, C.-Y., 2016. Fracture toughness of hydrogels: measurement and interpretation. Soft Matter 12, 8069–8086.
Long, R., Lefranc, M., Bouchaud, E., Hui, C.-Y., 2016. Large deformation effect in Mode I crack opening displacement of an agar gel: a comparison of experiment and theory. Extreme Mech. Lett. 9, 66–73.
Mao, Y., Anand, L., 2018. A theory for fracture of polymeric gels. J. Mech. Phys. Solids 115, 30–53.
Noselli, G., Lucantonio, A., McMeeking, R.M., DeSimone, A., 2016. Poroelastic toughening in polymer gels: a theoretical and numerical study. J. Mech. Phys. Solids 94, 33–46.
Peppas, N.A., Hilt, J.Z., Khademhosseini, A., Langer, R., 2006. Hydrogels in biology and medicine: from molecular principles to bionanotechnology. Adv. Mater. 18, 1345–1360.
Rivlin, R.S., Thomas, A.G., 1953. Rupture of rubber. I. Characteristic energy for tearing. J. Poly. Sci. 3, 291–318.
Sun, J.-Y., Zhao, X., Illeperuma, W.R.K., Chaudhuri, O., Oh, K.H., Mooney, D.J., Vlassak, J.J., Suo, Z., 2012. Highly stretchable and tough hydrogels. Nature 489, 133–136.
Suo, Z., 2012. Mechanics of stretchable electronics and soft machines. MRS Bull. 37, 218–225.
Tang, J., Li, J., Vlassak, J.J., Suo, Z., 2017. Fatigue fracture of hydrogels. Extreme Mech. Lett. 10, 24–31.
Wang, X., Hong, W., 2012. Delayed fracture in gels. Soft Matter 8, 8171–8178.
Yang, C.-H., Lin, Y.-Y, 2018. Time-dependent fracture of mode-I cracks in poroviscoelastic media. Eur. J. Mech. A 69, 78–87.
Yuk, H., Lin, S., Ma, C., Takaffoli, M., Fang, N.X., Zhao, X., 2017. Hydraulic hydrogel actuators and robots optically and sonically camouflaged in water. Nat. Commun. 8, 14230.
Zhao, X., 2014. Multi-scale multi-mechanism design of tough hydrogels: building dissipation into stretchy networks. Soft Matter 10, 672–687.